AIP | Journal of Renewable and Sustainable Energy

Validation of a FAST semi-submersible floating wind turbine numerical model with DeepCwind test data

Alexander J. Coulling, Andrew J. Goupee, Amy N. Robertson, Jason M. Jonkman, and Habib J. Dagher

Citation: Journal of Renewable and Sustainable Energy **5**, 023116 (2013); doi: 10.1063/1.4796197
View online: http://dx.doi.org/10.1063/1.4796197
View Table of Contents: http://scitation.aip.org/content/aip/journal/jrse/5/2?ver=pdfcov
Published by the AIP Publishing

JOURNAL OF RENEWABLE AND SUSTAINABLE ENERGY 5, 023116 (2013)

Validation of a FAST semi-submersible floating wind turbine numerical model with DeepCwind test data

Alexander J. Coulling,[1] Andrew J. Goupee,[1,a)] Amy N. Robertson,[2] Jason M. Jonkman,[2] and Habib J. Dagher[1]
[1]*Advanced Structures and Composites Center, University of Maine, Orono, Maine 04469-5793, USA*
[2]*National Renewable Energy Laboratory, 1617 Cole Boulevard, Golden, Colorado 80401-3393, USA*

(Received 7 November 2012; accepted 8 March 2013; published online 26 March 2013)

There are global efforts in the offshore wind community to develop reliable floating wind turbine technologies that are capable of exploiting the abundant deepwater wind resource. These efforts require validated numerical simulation tools to predict the coupled aero-hydro-servo-elastic behavior of such systems. To date, little has been done in the public domain to validate floating wind turbine simulation tools. This work begins to address this problem by presenting the validation of a model constructed in the National Renewable Energy Laboratory (NREL) floating wind turbine simulator FAST with 1/50th-scale model test data for a semi-submersible floating wind turbine system. The test was conducted by the University of Maine DeepCwind program at Maritime Research Institute Netherlands' offshore wind/wave basin, located in the Netherlands. The floating wind turbine used in the tests was a 1/50th-scale model of the NREL 5-MW horizontal-axis reference wind turbine with a 126 m rotor diameter. This turbine was mounted to the DeepCwind semi-submersible floating platform. This paper first outlines the details of the floating system studied, including the wind turbine, tower, platform, and mooring components. Subsequently, the calibration procedures used for tuning the FAST floating wind turbine model are discussed. Following this calibration, comparisons of FAST predictions and test data are presented that focus on system global and structural response resulting from aerodynamic and hydrodynamic loads. The results indicate that FAST captures many of the pertinent physics in the coupled floating wind turbine dynamics problem. In addition, the results highlight potential areas of improvement for both FAST and experimentation procedures to ensure accurate numerical modeling of floating wind turbine systems. © *2013 American Institute of Physics*. [http://dx.doi.org/10.1063/1.4796197]

I. INTRODUCTION

Numerical modeling is a vital component in many scientific disciplines that allows for quantitative representations of physical systems. Such representations are rarely perfect, but using different assumptions and idealizations, they make complex analyses and sound design practices possible. The simulation code used to create a numerical model must be verified and validated to ensure its predictions are representative and accurate, and that any deficiencies will not compromise the stability and structural integrity of an actual system that is designed based on the model. This is no different for floating offshore wind turbines. One of the most prevalent floating wind turbine analysis codes used to date is the National Renewable Energy Laboratory (NREL) simulator FAST.[1,2] This freely available numerical tool has been used in numerous floating wind turbine studies,[3–8] including the verification of a new code that permits large

[a)]Author to whom correspondence should be addressed. Electronic mail: agoupe91@maine.edu. Tel.: 207-581-2817.

angular deformations.[9] Altered versions of it have been used to investigate motion control[10–12] and other groups have used FAST coupled to either custom or commercial floating body hydrodynamics tools to analyze the coupled response of floating wind turbines.[13–18] To date, efforts have been made to verify FAST,[19–21] but little work has yet been accomplished in validating FAST against floating wind turbine test data. This is due in part to the scarcity of floating wind turbine test data openly available to the public. Limited data does exist from select model test endeavors;[14,15,22,23] however, only a few efforts have been made to validate a calibrated model[24,25] using FAST. In these works, the 1/50th-scale DeepCwind model test data[26–28] gathered at Maritime Research Institute Netherlands' (MARIN's) offshore wind/wave basin were utilized to create calibrated FAST models of the Glosten Associates-inspired[29] DeepCwind tension-leg platform and OC3-Hywind spar-buoy[30] floating wind turbine. These models were subsequently used to compare the simulation results with coupled response test data.

In this complementary work, similar efforts are made, albeit with the focus on a different platform configuration—the DeepCwind semi-submersible. The DeepCwind semi-submersible platform is a triangular, three-column design, and possesses a smaller fourth column located centrally to support a scale model of the horizontal-axis NREL 5-MW reference wind turbine.[31] This particular 1/50th-scale model floating wind turbine was extensively tested in MARIN's offshore basin under combined wind and wave loading, and the data recorded were targeted for the purposes of numerical model calibration and validation exercises. This paper outlines the construction and calibration of a FAST model of the DeepCwind semi-submersible floating wind turbine, and subsequently compares the simulation results to model test results. The validation efforts undertaken here focus on environmental conditions that are representative of those found in the Gulf of Maine.[32]

This paper is organized as follows. In Sec. II, a description of the numerical model is presented, including mass, elastic, aerodynamic, and hydrodynamic properties. Subsequently, Sec. III presents the procedures employed to calibrate certain facets of the FAST model. For example, tower-bending frequencies and viscous hydrodynamic drag, using select pieces of the test data are discussed. Section IV covers the comparison of the simulation and test data for steady wind only, dynamic wind only, steady wind free-decay, regular wave only, irregular wave only and lastly, combined irregular wave and dynamic wind conditions. In these following sections, it should be noted that indicial and direct notation are used interchangeably.

II. MODEL DESCRIPTION

In this section, a description of the DeepCwind semi-submersible floating wind turbine is presented. Froude scaling was used to create the 1/50th-scale model, shown in Fig. 1, and a variety of corresponding 1/50th-scale environmental loading conditions.

Descriptions of pertinent system properties will be given for the wind turbine, tower, floating platform, and mooring system. The properties, which will include mass, elastic, aerodynamic, and hydrodynamic quantities, are all presented at full-scale. It should also be noted that all test data and validation work is also presented at full-scale, as is customary for Froude-scale wave basin model testing. For more information regarding the scaling methods utilized to present the model test data at full-scale, please see the works of Jain *et al.*[8] and Martin *et al.*[33]

A. Wind turbine

This subsection describes pertinent properties of the rotor blades, hub, nacelle, and control system. The rotor diameter and hub height dimensions are identical to the NREL 5-MW reference wind turbine at 126.0 m and 90.0 m above the still water line (SWL), respectively. However, the wind turbine tower top mass is larger than the NREL turbine by 13.47%. This resulted from physical design constraints when producing the scale model, which necessitated a significant amount of electronic and instrumentation gear to be housed inside the nacelle.[34] After final design, accommodation of this equipment required a top-side mass of 397 160 kg, a total in excess of the desired 350 000 kg original target specification from the NREL 5-MW reference wind turbine. The gross properties of the model wind turbine are given in Table I. In

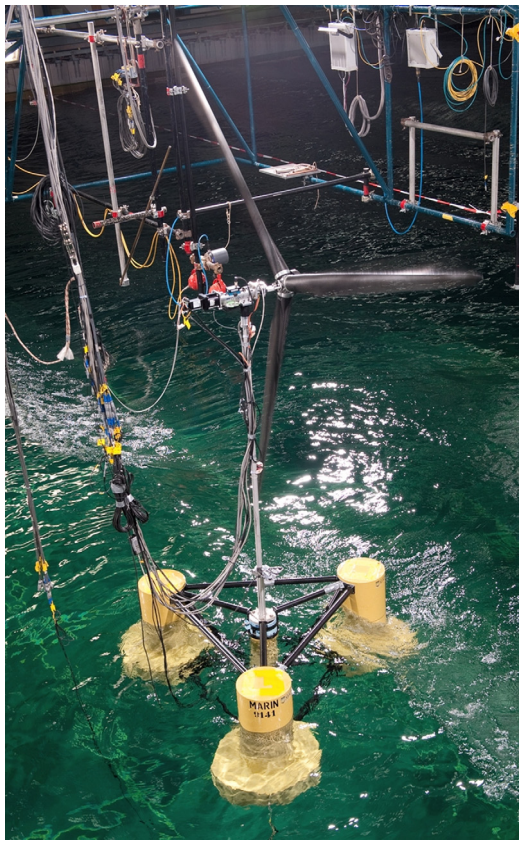

FIG. 1. Image of the 1/50th-scale DeepCwind semi-submersible floating wind turbine.

TABLE I. Wind turbine gross properties.

Rotor orientation, configuration	Upwind, 3 blades
Rotor, hub diameter	126.0 m, 3.0 m
Hub height above SWL	90.0 m
Height of tower-top flange above SWL	87.6 m
Overhang, shaft tilt, Precone	10.58 m, 0°, 0°
Vertical distance along tower centerline between tower top and shaft	2.4 m
Total tower-top mass	397 160 kg

TABLE II. Hub and nacelle gross properties.

Nacelle mass	274 940 kg
Nacelle center of mass (above tower)	2.4 m
Nacelle center of mass (downwind)	4.56 m
Nacelle roll inertia	284 100 kg m^2
Nacelle pitch inertia	22 440 000 kg m^2
Nacelle Yaw inertia	22 440 000 kg m^2
Hub mass	72 870 kg
Hub inertia about rotor axis	Negligible (0)

TABLE III. Blade gross properties.

Blade length	61.5 m
Blade mass	16 450 kg
Location of blade center of mass (measured from blade root)	23.4 m
Blade first mass moment of inertia	385 150 kg m
Blade second mass moment of inertia	13 940 000 kg m^2

Table II, additional details for the hub and nacelle required for generating a FAST numerical model are given. Note that the hub inertia about the rotor shaft axis is a very small contribution to the total rotor inertia and is taken to be zero. The experimentally derived rotor inertia and the total rotor inertia about the rotor axis utilized in the FAST model compare extremely well. A final detail worth noting is that the shaft tilt and blade precone are eliminated from both the physical and numerical models.

For the model tests, the rotor blades were designed to closely emulate the geometry of the NREL 5-MW reference wind turbine as is typical of a Froude-scaled model.[34] In addition, the total mass of the blade was targeted to be roughly equal to the NREL 5-MW reference wind turbine. However, the wind turbine blades were designed to be nearly rigid to eliminate the aeroelastic complexities resulting from flexible blades. As a result, the nine degrees of freedom (DOF) associated with blade flexibility in FAST are turned off for all calibration and validation efforts in this work. The gross wind blade properties are given in Table III and the distributed blade mass properties employed in the analyses are given in Table IV. Moving to Table V, details concerning the wind blade aerodynamics are presented, including blade twist, chord length, and airfoil designation. It is important to note that while the information in Table V is nearly identical to that for the NREL 5-MW reference wind turbine, the airfoil performance of the Froude-scaled blade geometry was significantly altered. This is because Froude scaling produces aerodynamic Reynolds numbers much smaller than what would be seen in a full-scale system. As such, new airfoil lift and drag coefficients were created for the model-scale wind

TABLE IV. Blade-distributed mass properties.

Radius (m)	Structural twist (deg)	Aerodynamic center (-)	Mass (kg/m)
1.50	13.308	0.250	5868.9
1.95	13.308	0.250	350.1
3.40	13.308	0.228	345.9
5.54	13.308	0.199	338.7
8.63	13.308	0.173	334.5
11.78	13.308	0.125	337.8
15.88	11.480	0.125	331.2
19.97	10.162	0.125	309.7
24.07	9.011	0.125	289.8
28.16	7.795	0.125	270.8
32.26	6.544	0.125	251.4
36.35	5.361	0.125	233.3
10.45	4.188	0.125	215.7
44.54	3.125	0.125	198.1
48.64	2.319	0.125	182.0
52.73	1.526	0.125	165.8
56.20	0.863	0.125	152.3
58.91	0.370	0.125	137.3
61.61	0.106	0.125	93.4
63.00	0.000	0.125	13.2

TABLE V. Blade-distributed aerodynamic properties.

Node radius (m)	Aerodynamic twist (deg)	Chord length (m)	Airfoil designation[a]
2.867	13.308	3.542	Cylinder
5.600	13.308	3.854	Cylinder
8.333	13.308	4.167	Cylinder
11.750	13.308	4.557	DU 40
15.850	11.480	4.652	DU 35
19.950	10.162	4.458	DU 35
24.050	9.011	4.249	DU 30
28.150	7.795	4.007	DU 25
32.250	6.544	3.748	DU 25
36.350	5.361	3.502	DU 21
40.450	4.188	3.256	DU 21
44.550	3.125	3.010	NACA 64-618
48.650	2.319	2.764	NACA 64-618
52.750	1.526	2.518	NACA 64-618
56.167	0.863	2.313	NACA 64-618
58.900	0.370	2.086	NACA 64-618
61.633	0.106	1.419	NACA 64-618

[a]DU = Delft University, NACA = National Advisory Committee for Aeronautics.

turbine through a calibration process that employed model test wind turbine performance data. The details of this procedure are outlined in the calibration section of this paper.

Moving to the operating details of the wind turbine, the control system used for the model wind turbine was very basic compared to the variable-speed, active blade-pitch systems encountered in many existing commercial-scale wind turbines. The tested system did not use variable-speed control or active pitch control in an effort to manage the complexity of the model testing campaign. In operational test modes, the blades on the turbine were each fixed at a collective pitch of 6.4° and in parked test modes the blades were each fixed at 85°. Because of the aforementioned altered airfoil performance of the wind blades, the collective blade-pitch values utilized for operating and feathered modes differ from those employed in Ref. 31. During each test, the rotor speed was held constant, although the speed did change from test to test. Table VI shows the various environmental and operating conditions for the model wind turbine studied in this work. Aside from a range of environments with an operating wind turbine, this work considered one extreme environment with a parked wind turbine and a mean wind speed of 30.5 m/s corresponding to a 100-year event in the Gulf of Maine.[32]

B. Tower

The tower for the DeepCwind semi-submersible platform was designed to emulate the fundamental bending frequencies of the OC3-Hywind tower[30] when supporting the previously

TABLE VI. Wind turbine operating parameters.

Mean wind speed (m/s)	Reference height (m)	Wind condition	Rotor speed (RPM)	Collective blade pitch angle (deg)
7.32	90.0	Steady	4.95	6.4
8.94	90.0	Steady	5.66	6.4
11.23	90.0	Steady	7.78	6.4
16.11	90.0	Steady	9.19	6.4
21.80	90.0	Steady	12.73	6.4
30.50	90.0	Steady	0.0	85.0
16.98 (20.60)	10.0 (90.0)	Dynamic	12.73	6.4

TABLE VII. Gross tower properties.

Tower height	77.6 m
Tower base elevation above SWL	10.0 m
Tower top elevation above SWL	87.6 m
Total mass	302 240 kg
Center of mass above SWL	44.6 m

described wind turbine mounted atop the OC3-Hywind spar-buoy. Successful achievement of this target is demonstrated in Ref. 34.

The mass and stiffness properties of the tower were calculated using the tower geometry and material properties of aluminum, of which the tower is made. As can be seen in Fig. 1, there was a significant bundle of instrumentation cables that runs along a majority of the tower for the physically tested model. The weight of these cables that the floating platform had to support was calculated during testing, and this additional mass was evenly distributed along the entire length of the tower for numerical modeling. The cables were assumed to add negligible bending stiffness to the tower. The gross properties of the tower are given in Table VII and the distributed properties are found in Table VIII. Note that Table VIII only provides bending stiffness and excludes tower torsional and extensional stiffnesses as these quantities are not utilized by the FAST code.

In addition to distributed properties, FAST also requires the first two modes of vibration for both fore-aft and side-side bending as well as modal damping quantities. The generation of mode shapes, estimation of modal damping, and reconciliation of FAST tower response with test data will be covered in the calibration section of this work.

C. Floating platform

The floating platform for this model is a semi-submersible. It is considered to be buoyancy-stabilized because rotational displacements induce large buoyant-restoring forces from the volumes of water that are displaced. Dimensioned drawings of the DeepCwind semi-submersible platform are given in Fig. 2 along with the coordinate system employed in this study. The platform is made up of three offset columns with larger diameter lower bases, one center support column for the turbine, and a series of horizontal and diagonal cross bracing. The 1.6-m-diameter cross bracing consists of two sets of three pontoons connecting the outer columns with each other, two sets of three pontoons connecting the outer columns to the center column, and three diagonal braces connecting the top of the outer column to the bottom of the center column. An overview of the full-scale dimensions and gross properties of the platform are given in Table IX. Concerning platform flexibility, the 1/50th-scale platform was designed to be very stiff and was assumed to be rigid for the analyses conducted in this work. This is consistent with the modeling

TABLE VIII. Tower distributed properties.

Elevation (m)	Mass (kg/m)	Fore-aft stiffness (Nm^2)	Side-side stiffness (Nm^2)
10.00-10.31	55 671.5	1.123×10^{12}	1.123×10^{12}
10.31-18.54	4599.0	1.123×10^{12}	1.123×10^{12}
18.54-21.56	5808.1	1.371×10^{12}	1.371×10^{12}
21.56-22.26	16 044.3	1.371×10^{12}	1.371×10^{12}
22.26-81.63	2982.9	2.485×10^{11}	2.485×10^{11}
81.63-82.87	5128.5	2.485×10^{11}	2.485×10^{11}
82.87-83.49	11 821.4	2.485×10^{11}	2.485×10^{11}
83.49-84.42	10 433.7	2.485×10^{11}	2.485×10^{11}
84.42-87.60	5710.8	1.104×10^{12}	1.104×10^{12}

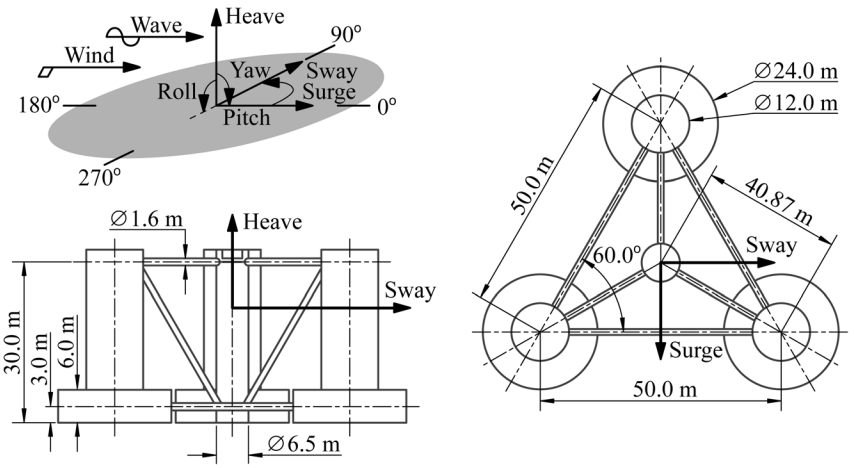

FIG. 2. Coordinate system and dimensions of the DeepCwind semi-submersible platform.

approach employed in FAST.[2] A full-scale platform built with these dimensions would likely have some compliance and therefore require larger bracing components to be considered rigid. It is important to note that the model tests performed were intended to capture the global performance characteristics of a generic semi-submersible platform, not to analyze an optimal design. Certainly more efficient semi-submersible designs can be created through optimization.

Regarding hydrodynamics, FAST implements a linear, time-domain formulation in which the problem is separated into three separate problems: hydrostatics, diffraction, and radiation.[2,35,36] The quantities required for executing the time-domain hydrodynamic load simulation are obtained from WAMIT,[37] a three-dimensional frequency-domain potential-flow numerical panel method. For WAMIT analysis, a higher-order representation geometric description file for the DeepCwind semi-submersible platform was created using MultiSurf.[38] In the higher-order geometric description, the velocity potential on the body surface is represented using B-splines. One geometric plane of symmetry was exploited in the analysis, and the average panel size utilized was 2.0 m. To further improve the accuracy of the WAMIT results, options were selected to integrate the logarithmic singularity analytically, solve the linear system of equations using a direct solver, and remove the effects of irregular frequencies by manually paneling the free surface. These settings were beneficial because of the requirement for high-frequency output for time-domain analysis. The semi-submersible platform was analyzed in its undisplaced position and with a water depth of 200.0 m. The origin for the analysis was taken to be the intersection of the platform centerline and waterline because this point coincides with the location of FAST platform DOF. As such, all hydrodynamic quantities in this section are referenced from this point.

With the numerical solution parameters established, the output of the WAMIT analysis is now presented and discussed. The linear hydrostatic restoring forces account for contributions due to system weight and center of gravity location, buoyancy and center of buoyancy location,

TABLE IX. Platform gross properties.

Depth to platform base below SWL (total draft)	20.0 m
Elevation to platform top (tower base) above SWL	10.0 m
Platform mass, including ballast	13 444 000 kg
Displacement	13 986.8 m^3
Center of mass (CM) location below SWL along platform centerline	14.4 m
Platform roll inertia about CM	8.011×10^9 kg m^2
Platform pitch inertia about CM	8.011×10^9 kg m^2
Platform Yaw inertia about platform centerline	1.391×10^{10} kg m^2

and lastly, water plane stiffness. In FAST, the contribution due to weight is handled separately and the hydrostatic restoring force is characterized via a stiffness matrix, C_{ij}^H, which includes only buoyancy and water plane effects. The hydrostatic forces F_i^H are computed as

$$F_i^H = \rho g V_o \delta_{i3} - C_{ij}^H q_j, \quad i,j = 1,2,\ldots,6, \tag{1}$$

where ρ is the density of water ($1025.0\,\mathrm{kg/m^3}$), g is the local acceleration due to gravity ($9.80665\,\mathrm{m/s^2}$), V_o is the displaced volume in the undisplaced position, δ_{i3} is the Kronecker delta, q_j are the six rigid-body DOF located at the waterline and C_{ij}^H is

$$\boldsymbol{C}^H = \begin{bmatrix} 0 & 0 & 0 & 0 & 0 & 0 \\ 0 & 0 & 0 & 0 & 0 & 0 \\ 0 & 0 & 3.836\,\mathrm{N/m} & 0 & 0 & 0 \\ 0 & 0 & 0 & -377.6\,\mathrm{Nm/rad} & 0 & 0 \\ 0 & 0 & 0 & 0 & -377.6\,\mathrm{Nm/rad} & 0 \\ 0 & 0 & 0 & 0 & 0 & 0 \end{bmatrix} \times 10^6. \tag{2}$$

The diffraction forcing, which considers the hydrodynamic loads associated with incident waves, is characterized by wave frequency- and direction-dependent first-order transfer functions, $X_i(\omega,\beta)$, where ω is the wave frequency and β is the wave direction. The complex valued $X_i(\omega,\beta)$ vector contains the platform forces and moments per unit wave amplitude and the interplay of the real and imaginary components determine the phase lag between the wave crest and the peak forces. A plot of the first-order transfer function magnitudes and phase angles for a zero degree wave heading is given in Fig. 3.

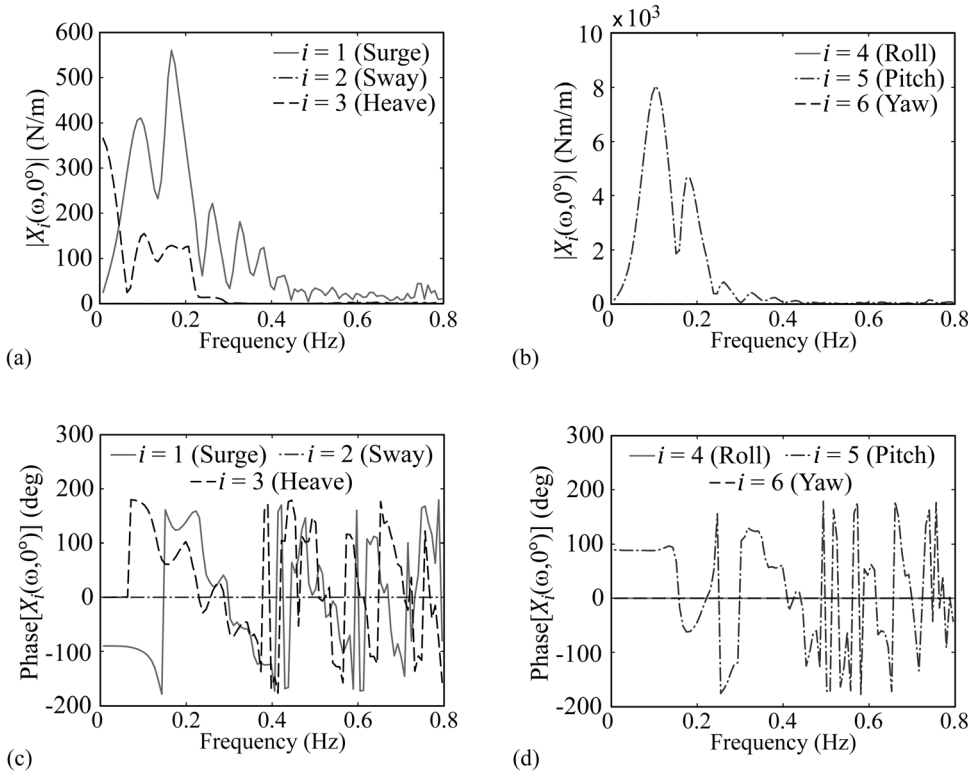

FIG. 3. Plots of first-order transfer functions at a zero-degree wave heading for (a) forces and (b) moments, along with phase lag angles for forces and moments in (c) and (d), respectively, as a function of frequency.

The last hydrodynamic force considered in the linear implementation is the radiation force that accounts for platform forces associated with the oscillation of the platform. To compute forces associated with radiation in the time domain, FAST requires knowledge of the infinite-frequency, added-mass matrix, $A_{ij}(\infty)$, and the oscillation-frequency-dependent damping matrix, $B_{ij}(\omega)$.[2] The WAMIT-derived, infinite-frequency, added-mass matrix for the DeepCwind semi-submersible platform is

$$\boldsymbol{A}(\infty) = \begin{bmatrix} 6.504 & 0 & 0 & 0 & -85.44\,\text{m} & 0 \\ 0 & 6.504 & 0 & 85.44\,\text{m} & 0 & 0 \\ 0 & 0 & 14.71 & 0 & 0 & 0 \\ 0 & 85.44\,\text{m} & 0 & 7257\,\text{m}^2 & 0 & 0 \\ -85.44\,\text{m} & 0 & 0 & 0 & 7257\,\text{m}^2 & 0 \\ 0 & 0 & 0 & 0 & 0 & 4894\,\text{m}^2 \end{bmatrix} \times 10^6\,\text{kg}. \quad (3)$$

Plots of the non-zero damping-matrix components for the DeepCwind semi-submersible platform as a function of frequency are given in Fig. 4.

In addition to linear hydrodynamic forces, a quadratic drag model is implemented in this work to account for flow-separation-induced drag. FAST has the ability to compute drag forces using Morison's equation for the main column; however, the formulation does not permit inclusion of all the members of the semi-submersible platform. Therefore, the coefficients employed in this quadratic drag model are determined from experimental data to represent the additional damping present in the system. A discussion of the quadratic drag model and derivation of coefficients is presented in the calibration section of this paper.

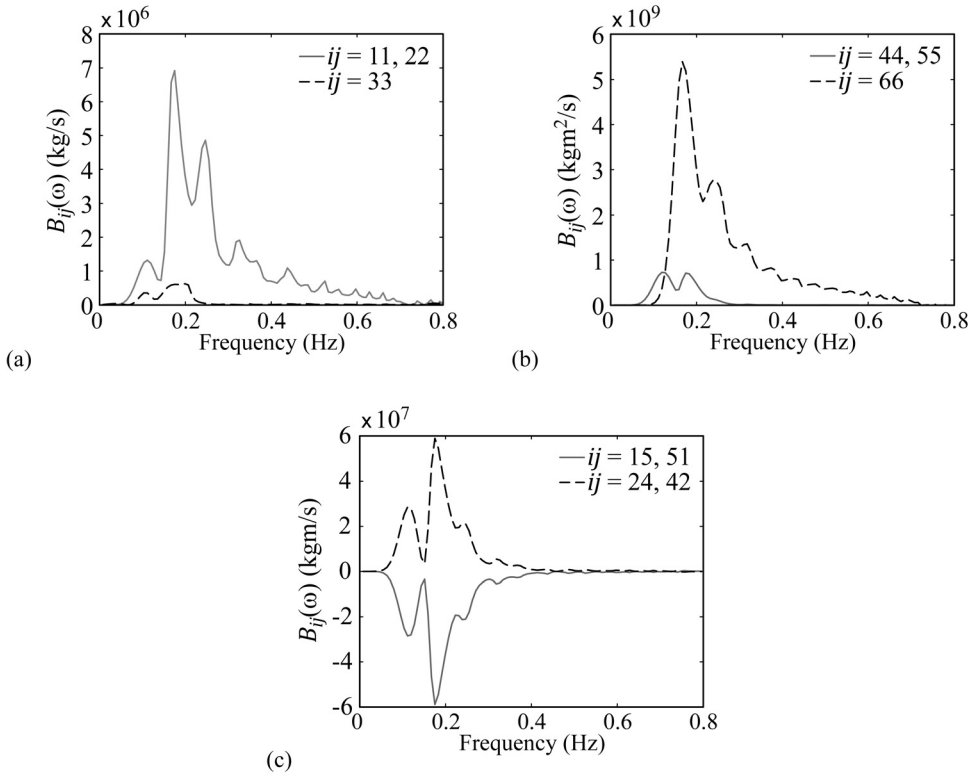

FIG. 4. Plots of the nonzero entries of the damping matrix as a function of frequency for the (a) translational modes, (b) rotational modes, and (c) coupled translation-rotation modes.

D. Mooring system

The mooring system for the DeepCwind semi-submersible platform consists of three slack, catenary lines that provide the primary global restoring forces for motion in surge, sway, and yaw, and additional, albeit marginal, global restoring forces for heave, roll, and pitch motion. The default quasi-static mooring module from FAST is employed in this work, and the details of how the non-linear catenary equations are solved can be found in Ref. 2. The relevant information for the mooring system is found in Table X. The three mooring lines are orientated at 60°, 180°, and 300° (lines 1, 2, and 3, respectively) about the heave axis with 0° being aligned with the surge axis. A comparison of the numerical model and the tuned physical mooring system employed for testing is covered in the calibration section.

III. MODEL CALIBRATION

In this section, the calibration of various tunable aspects of the wind turbine model is presented. These tunable aspects rely on test information from simple, fundamental tests of the floating wind turbine that focus on characterizing a particular facet of system behavior. These tests, called system identification tests, are used to tune the FAST wind turbine aerodynamics, first tower-bending mode frequencies, and viscous damping parameters. The tests also verify the system restoring forces provided by the mooring system. The data employed for use in the calibration process can be found in Ref. 28. This step is necessary because of unknown testing parameters and some imperfections in the numerical model.

A. Wind turbine performance

During model testing, the low wind speeds of the Froude-scale environment created Reynolds numbers that were nearly three orders of magnitude lower than full-scale. This resulted in altered airfoil lift and drag performance with overall lower thrust loads and power production relative to the full-scale NREL 5-MW reference wind turbine for a given wind speed. Because thrust loading is the major aerodynamic driver for global motion of the system, higher wind speeds were selected for testing, which yielded proper, Froude-scale rotor thrust values. The details of the wind turbine performance deficiency and accompanying adjustments are discussed in Ref. 33.

For completeness, it is noted that a high-quality wind environment was generated in MARIN's offshore basin using a suspended rectangular rack with 35 fans, a series of screens, and an elliptically shaped nozzle. The nozzle outlet used was 200 m wide and 150 m tall (full scale), this being larger than the rotor swept area. Turbulence intensity at the hub location was measured to be 4% and modestly higher at the boundaries of the outlet nozzle. Swirl in the flow field was less than 1% of the free stream velocity. A more thorough description of the wind generation machine can be found in Ref. 26.

TABLE X. Mooring system properties.

Number of mooring lines	3
Angle between adjacent lines	120°
Depth to anchors below SWL (water depth)	200 m
Depth to fairleads below SWL	14 m
Radius to anchors from platform centerline	837.6 m
Radius to fairleads from platform centerline	40.868 m
Unstretched mooring line length	835.5 m
Mooring line diameter	0.0766 m
Equivalent mooring line mass density	113.35 kg/m
Equivalent mooring line mass in water	108.63 kg/m
Equivalent mooring line extensional stiffness	753.6×10^6 N

For numerical modeling in FAST, the altered performance of the wind turbine necessitated a new aerodynamic model because the one associated with the standard NREL 5-MW reference wind turbine was no longer applicable. To begin the process, new coefficients of lift and drag for the airfoils of Table V at various angles of attack were generated by building a model of the airfoils in XFOIL, a high-order, viscous-analysis panel code.[39] The resulting lift and drag curves were then processed using NREL's AirfoilPrep tool[40] to expand the data over the entire 360° range of possible angles of attack required by FAST. This produced simulation results that correlated poorly to model test data because of the questionable applicability of XFOIL solutions for the separated flows experienced in the tested model wind turbine. Hence, the XFOIL lift and drag curves for the airfoils were parameterized and tuned using multi-objective genetic algorithm optimization techniques (e.g. see Ref. 41) to simultaneously minimize the error between FAST simulations and test data curves for the wind turbine thrust and power as a function of rotor speed under a steady hub height wind speed of 21.80 m/s. Options utilized in FAST for the optimization included disabled dynamic stall, elimination of the pitching moment model, selection of the swirl equilibrium inflow model, and selection of the Prandtl tip- and hub-loss models.[1] The air density was taken to be 1.225 kg/m^3. The wind profile generated in the wind/wave basin used a simple wind file, which contained one hub-height wind speed for steady winds and a time-series of varying wind speeds for dynamic winds studied later in this work. To best represent this wind profile, the measured hub height wind speed was multiplied by a factor of 0.952 and a vertical power law wind shear exponent of 0.0912 was employed. These parameters yielded the best comparison between measured hub-height wind speeds and information gleaned from spatial surveys of the wind generation machine output used for testing. Details of the wind machine surveys can be found in Refs. 26 and 28. Regarding parameterization of the airfoil coefficients, variables were introduced that permitted perturbations of lift curve slope and zero-lift angle of attack, as well as more moderate alterations of the lift curve stall point, lift curve post-stall behavior, and general nature of the drag coefficients. Because the multi-objective optimization generated several pareto-optimal solutions, a solution was chosen for use in the numerical model that exhibited nearly identical thrust behavior to the test model and a reasonably fair prediction of wind turbine power. This bias towards more accurately capturing the thrust response is due to the aforementioned fact that wind turbine thrust is the aerodynamic driver in global motion and load response.

A comparison of the calibrated FAST and model test wind turbine performance is given in Fig. 5. In addition, Table XI shows the thrust values corresponding to the steady wind cases of Table VI. As can be seen in Fig. 5 and Table XI, the thrust behavior that is critical for properly simulating global response is captured very well by the calibrated FAST wind turbine model. In addition, the range of thrust values captured during testing is very similar to the true NREL 5-MW reference wind turbine with peak thrust loads in the neighborhood of 800 kN, as shown in Table XI. It should be noted that the peak thrust load occurs at a different wind speed for model-scale compared to an ideal full-scale wind turbine because of the inherently low Reynolds numbers seen at model-scale. The aerodynamic lift (C_L) and drag (C_D) coefficients corresponding to the calibrated wind

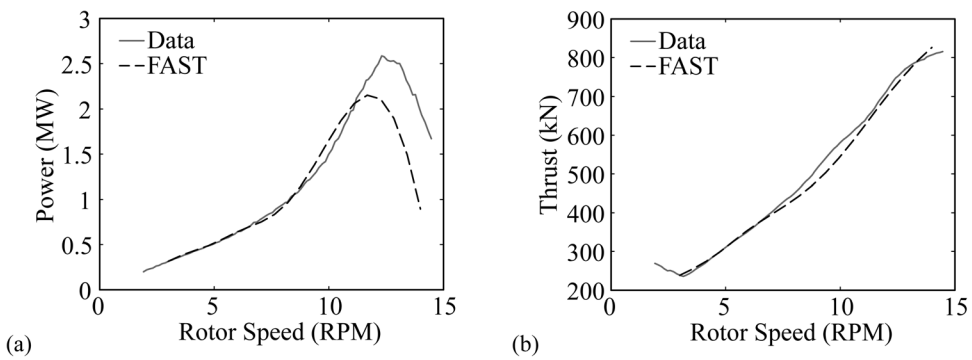

FIG. 5. Comparison of calibrated FAST and tested wind turbine performance as a function of rotor speed for (a) rotor power and (b) thrust under steady 21.80 m/s winds.

TABLE XI. Comparison of calibrated FAST model and tested wind turbine thrust.

Mean wind speed (m/s)	Rotor speed (RPM)	Tested thrust (kN)	FAST thrust (kN)
7.32	4.95	126.1	102.6
8.94	5.66	156.9	143.4
11.23	7.78	202.7	247.2
16.11	9.19	381.7	413.0
21.80	12.73	749.8	779.3
30.50	0	156.8	153.2

turbine model for the airfoil sections noted in Table V are given in Fig. 6. For the cylinder section, the lift coefficient was set to 0.0 and the drag coefficient to 1.0 for all angles of attack.

B. Tower mode shapes and frequencies

To model tower flexibility, FAST's modal representation requires the first two elastic bending mode shapes for both the fore-aft and side-side tower-bending DOF. Factors that influence

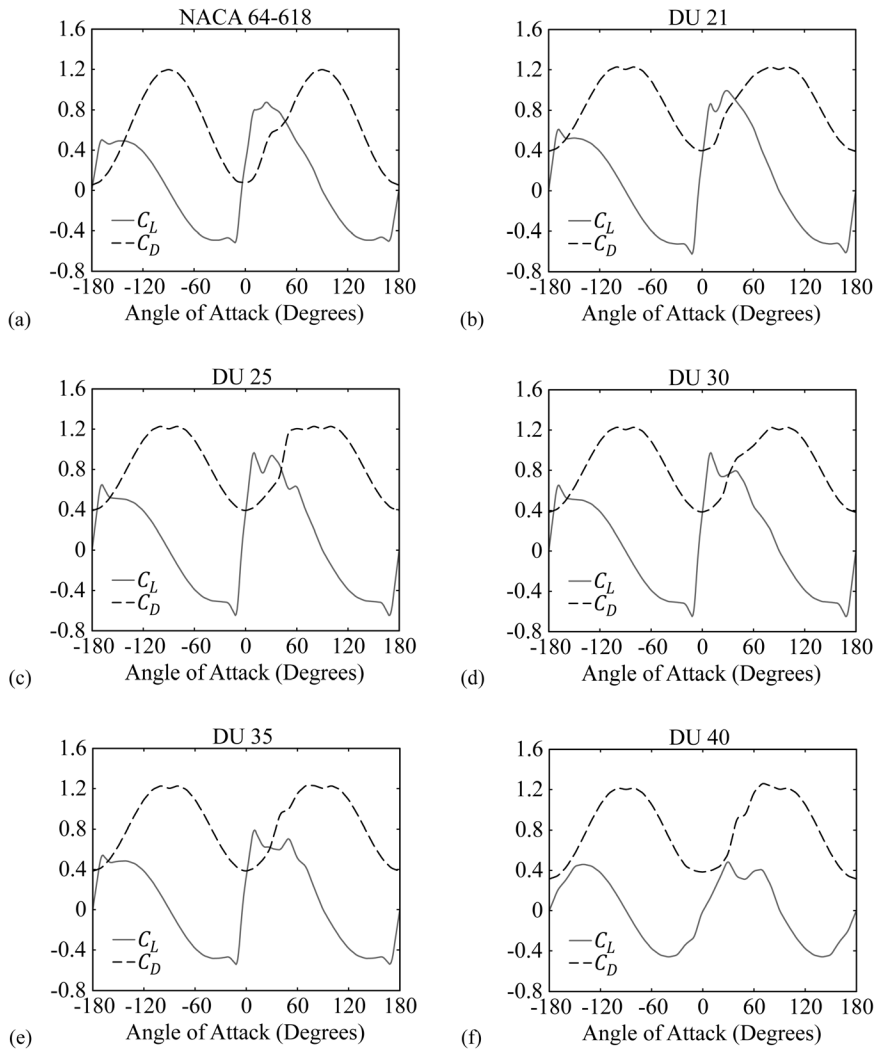

FIG. 6. Plots of airfoil lift and drag coefficients at low Reynolds number for (a) NACA 64-618, (b) DU 21, (c) DU 25, (d) DU 30, (e) DU 35, and (f) DU 40 airfoils for the tuned FAST aerodynamic model.

the tower vibration mode shapes include distributed tower mass and stiffness properties, tower-top mass properties, gravity, floating foundation mass, added-mass, hydrostatic stiffness, and mooring stiffness properties.

To estimate these mode shapes, a simple custom finite-element tool was developed that employed three-dimensional Euler-Bernoulli beam elements (e.g., see Ref. 42) to discretize the tower. After inputting the aforementioned distributed tower, turbine mass, platform mass, and stiffness properties, the finite-element system mass and stiffness matrices were constructed and the eigenvalue problem was solved using standard techniques. The appropriate first and second bending mode shapes for the fore-aft and side-side tower-bending DOF were extracted, and normalized ninth-order mode shapes were constructed for input into FAST. The mode shapes are plotted in Fig. 7. The higher-order polynomials were employed because the standard sixth-order polynomials do not accurately capture the finite-element-estimated mode shapes resulting from the multiple discontinuities in the distributed tower properties.

Upon inserting the mode shapes into the FAST model and running a linearization analysis to determine the tower-bending frequencies,[1] it was found that the finite element and FAST tower frequencies were in relative agreement. However, the FAST fundamental tower-bending frequencies were approximately 10% higher than measured from hammer tests conducted on the DeepCwind semi-submersible. While it is unknown why the discrepancy occurred, it could be due to, for example, a greater compliance between the tower base and floating platform connection for the DeepCwind semi-submersible. Another possibility is that the DeepCwind semi-submersible was the last specimen tested and that the base, mid-tower, and top joints on the tower could have relaxed or loosened slightly after weeks of double-shift, repeated testing. In any event, the tower stiffness properties of Table VIII were reduced by 21.0% to better match the test data. The individual fore-aft and side-side fundamental tower-bending natural frequencies were fine tuned to match test data by adjusting FAST's modal stiffness tuners. The final stiffness tuner values used in fore-aft and side-side DOFs were 0.905 and 1.049, respectively. After final calibration of the tower stiffnesses, the FAST fore-aft and side-side tower-bending frequencies match experimental measurements and are 0.35 Hz and 0.38 Hz, respectively.

In addition to mode shapes, FAST also requires damping ratios for each of the tower bending modes. The damping ratios of the tower-bending modes were estimated using the half-power bandwidth method (e.g., see Ref. 43) in conjunction with acceleration records from hammer tests. A value of 2.1% was determined for first mode fore-aft and side-side structural damping, and a value of 1.5% was determined for second mode fore-aft and side-side structural damping.

C. Hydrodynamic viscous damping

For the DeepCwind semi-submersible platform, flow-separation-induced drag is a large component of the total hydrodynamic damping. As such, the linear time-domain radiation damping included in FAST was augmented with a quadratic damping model that captures the effects of this viscous damping. The platform viscous damping forces and moments, F_i^v, are computed as

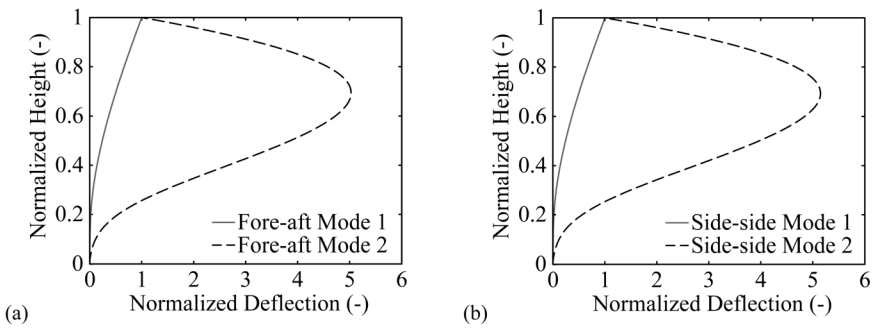

FIG. 7. Plots of the FAST normalized ninth-order tower mode shapes for (a) fore-aft and (b) side-side bending DOF.

TABLE XII. Platform quadratic drag coefficients.

DOF	Global quadratic coefficient
Surge	1.25×10^6 Ns^2/m^2
Sway	0.95×10^6 Ns^2/m^2
Heave	3.88×10^6 Ns^2/m^2
Roll	3.35×10^{10} Nms^2/rad^2
Pitch	3.35×10^{10} Nms^2/rad^2
Yaw	1.15×10^{10} Nms^2/rad^2

$$F_i^v = -B_{ij}^v \dot{q}_j |\dot{q}_j|, \quad i,j = 1,2,\ldots,6, \tag{4}$$

where B_{ij}^v are the quadratic damping coefficients, q_j are the six rigid-body DOF located at the waterline, and a superimposed dot indicates the first time derivative. This model assumes no directional coupling of drag terms, so only diagonal terms of B_{ij}^v are nonzero.

The coefficients B_{ij}^v were determined using the rigid-body motion free-decay tests conducted in the wind/wave basin. Simulation free-decay results for each of the six platform degrees of freedom were tuned by varying B_{ij}^v for each DOF until fair agreement existed between FAST and the test data. The free-decay test data were also employed to estimate the additional global surge stiffness provided by the cable bundle shown in Fig. 1. The computed additional surge stiffness is 7.39 kN/m and was employed in all subsequent numerical experiments. The derived global drag coefficients are given in Table XII. A comparison of the FAST predictions and test data for free-decay damping ratio response is given in Fig. 8 for platform surge, heave, and pitch DOF. The free-decay damping ratios are presented as the damping ratio over one cycle as a function of initial cycle amplitude. As can be seen in the figure, the overall nonlinear hydrodynamic damping behavior is captured very well for small to moderate amplitude oscillations. For large amplitudes, the quadratic damping model employed here overpredicts heave and pitch damping and under-predicts surge damping.

D. Mooring restoring forces

Unlike the previously discussed quantities in this calibration section, the mooring system parameters were not tuned in order to reconcile differences in system restoring forces between FAST and the test data. In fact, the mooring module in FAST was utilized to set the target global restoring forces for the model test, and the physical model was tuned to reach these targets. The physical mooring system that was tested, which was full length and not truncated, utilized chain that yielded the correct mooring line wet weight with carefully selected springs placed at the anchors to capture the appropriate extensional stiffness of the mooring line. A comparison of mooring restoring in surge and sway DOF for both FAST simulations and test

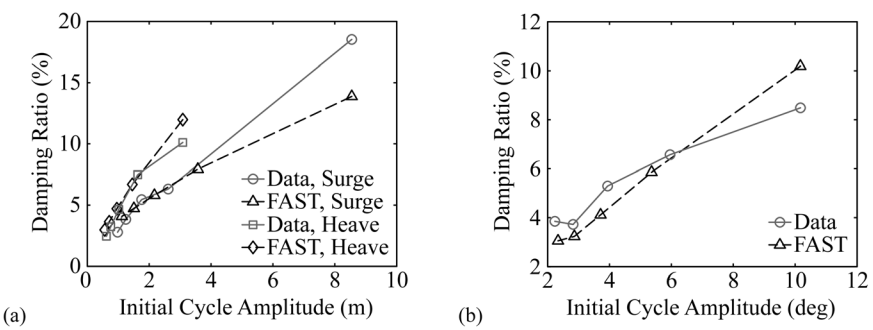

FIG. 8. Comparisons for FAST prediction and test data free-decay damping ratios for (a) surge and heave as well as (b) pitch DOF.

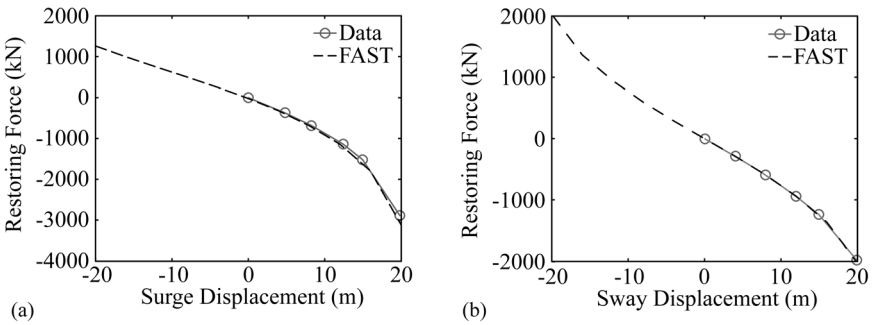

FIG. 9. Comparisons for FAST prediction and test data for (a) surge mooring restoring force and (b) sway mooring restoring force.

results are given in Fig. 9. As can be seen in the figure, there is excellent agreement between the simulation and test data. There is further evidence that the numerical model mooring system stiffness is correct; in addition to hydrostatic stiffness, system mass, and added-mass, a comparison of FAST simulation and tested rigid-body motion natural periods is given in Table XIII. As the table shows, the agreement between the simulation and test data is excellent.

IV. MODEL VALIDATION

In this section, the output of the calibrated FAST model from Sec. II will be compared to wind/wave basin model test data for the DeepCwind semi-submersible. Cases that are considered include steady wind only, dynamic wind only, free-decay under steady wind, regular waves only, irregular white noise waves only, and lastly, combined dynamic wind and irregular wave conditions. This systematic approach allows for an easier identification of root causes for discrepancies between test data and FAST simulations. This noted, the results highlight the many merits of FAST's predictive capabilities in addition to potential shortcomings in the test data, as well as possible areas of improvement for FAST. Lastly, it should be noted that all the relevant global motion results presented in subsequent sections are given with respect to the center of gravity of the total system. The FAST global motions results are initially obtained at the waterline and have been transformed accordingly.

A. Steady wind only

Simulations of the DeepCwind semi-submersible platform subjected to the six steady wind environments noted in Table VI were conducted and compared to model test data. All winds were directed along the positive surge direction. As was done in the calibration portion for tuning wind turbine aerodynamics, the steady wind files required for simulation were produced by multiplying the mean hub height wind speed of Table VI by 0.952 and using a wind shear coefficient of 0.0912. The metric targeted for comparison between simulation and test data was the steady-state solution. While the model test cases were run for 1 h, the FAST simulations results

TABLE XIII. Comparison of FAST prediction and test data for the six rigid-body motion natural periods.

DOF	FAST (s)	Data (s)
Surge	107	107
Sway	113	112
Heave	17.3	17.5
Roll	26.7	26.9
Pitch	26.8	26.8
Yaw	82.7	82.3

were terminated at 2000 s because any significant transient global motions had diminished well in advance of this time.

For these particular loading scenarios, responses associated with surge and pitch motion receive the most excitation. As such, the mean platform surge and pitch angle are presented in Fig. 10, as are the tower base fore-aft bending moment and mooring line 2 fairlead tension. As can be seen in the figure, the comparison between the simulation and test data is quite favorable. One obvious trend shown in the figure is that FAST appears to under-predict the mean surge offset with the largest discrepancies, from a percentage point of view, occurring at low operational winds and at the highest wind speed where the blades are feathered and the rotor is parked. For these aforementioned conditions, the thrust load on the rotor is low and aerodynamic drag loads on the tower, floating platform, and instrumentation cable bundle, which are not included in this FAST model, may be contributing a substantial portion to the total overall system surge force. Because the comparison between FAST and the test data is quite good with regard to tower-base fore-aft bending moment, it is likely that the largest contribution is additional aerodynamic drag on the platform. In addition, this situation is exacerbated by the fact that the low rotor thrust coefficient, resulting from poor airfoil performance[33] at the low test Reynolds numbers, required higher wind speeds to produce an equivalent full-scale rotor thrust, thus creating greater drag on non-rotor structures (e.g., the platform) than would be seen in a true full-scale system. Lastly, the surge-restoring stiffness is in general quite low, yielding significant discrepancies in surge position despite only small differences in total system surge loading. As an example, even in the 30.5 m/s case where the worst discrepancy occurs, the 1.84 m difference in predicted surge position is caused by a relatively small 140 kN difference in overall system surge loading. Unlike the total system surge loading, the system overturning moment leading to pitch and tower bending moment response is dominated by the rotor, because it is higher above the SWL than the center of pressure for the tower, cable bundle, or platform. The FAST rotor thrust is fairly well predicted as a result of the calibration shown in Fig. 5, so it stands to reason that the simulation and test data pitch responses are very similar in Fig. 10. In addition, while the agreement for mean pitch offset is good, there is an

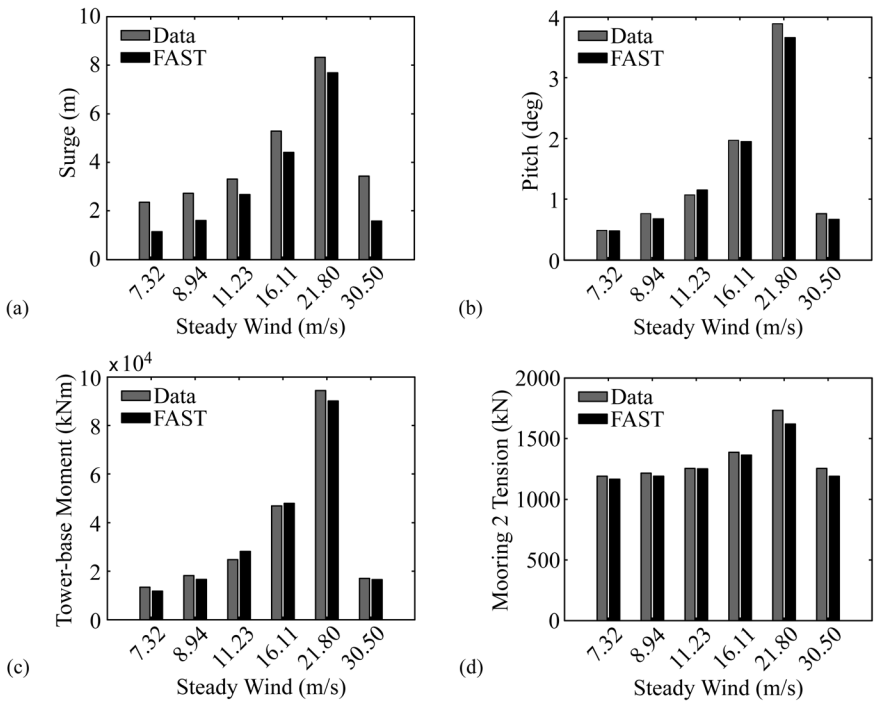

FIG. 10. Comparison of simulation and test data steady-state response under steady winds for (a) surge, (b) pitch, (c) tower-base fore-aft bending moment, and (d) mooring line 2 fairlead tension.

under-prediction by FAST that is consistent with the simulation, ignoring the aforementioned, additional aerodynamic drag loads.

B. Steady wind free-decay

As the second phase of model validation, the ability of FAST to capture the wind turbine rotor's aerodynamic damping forces is assessed. This was evaluated by simulating free-decay while the wind turbine was operating in a steady wind, with no waves, and comparing the motion response between FAST simulations and test data. The surge and pitch platform DOF, which are most affected by aerodynamic forces on the wind turbine, are the focus of this section.

For the two free-decay scenarios investigated, the wind turbine was subjected to the third smallest steady wind from Table VI. Consistent with the treatment of the wind in previous simulations, the steady wind file was generated by multiplying the experimentally measured 11.23 m/s wind by 0.952 and utilizing a 0.0912 wind shear exponent. Recall that this was done to best replicate the experimental wind velocity distribution using only a single, steady wind file. A comparison of the simulation and test data surge and pitch motion damping ratios as a function of initial cycle amplitude is given in Fig. 11 for the no-wind and 11.23 m/s wind cases. For both surge and pitch free-decay, regardless of the wind condition, the comparison between FAST and the test data is quite good overall, especially for small to moderate motion amplitudes. More importantly, FAST accurately captures the additional motion damping, approximately 1% in surge and 3% in pitch for this scenario, provided by the operating wind turbine in steady winds.

C. Dynamic wind only

To complete the wind only comparisons, the response of the DeepCwind semi-submersible subjected to a strong, dynamic wind in the absence of waves was simulated and compared to experimental data. The wind field, which was temporally dynamic, followed a National Petroleum Directorate (NPD) spectrum[44] and was oriented along the positive surge direction. In the wind/wave basin, the temporally dynamic NPD wind possessed a mean wind speed at hub height of 20.6 m/s, a standard deviation of 2.04 m/s, a maximum wind speed of 28.7 m/s, and a minimum wind speed of 12.9 m/s. A power spectral density (PSD) plot of the wind time-series, which was 3 h in length, is given in Fig. 12. For simulation, a dynamic wind file was created in the usual manner by multiplying the recorded hub height wind velocity time history by 0.952 and utilizing a wind shear exponent of 0.0912 to better represent the measured spatial distribution of wind generated during testing. This yielded winds for simulation with a mean of 19.6 m/s, a standard deviation of 1.94 m/s, a maximum of 27.4 m/s, and a minimum of 12.3 m/s at the hub-height location (90 m above SWL).

A comparison of the FAST predictions and experimental data for platform pitch and mooring line 2 fairlead tension is given in Figs. 13 and 14. Fig. 13 provides comparisons via PSDs,

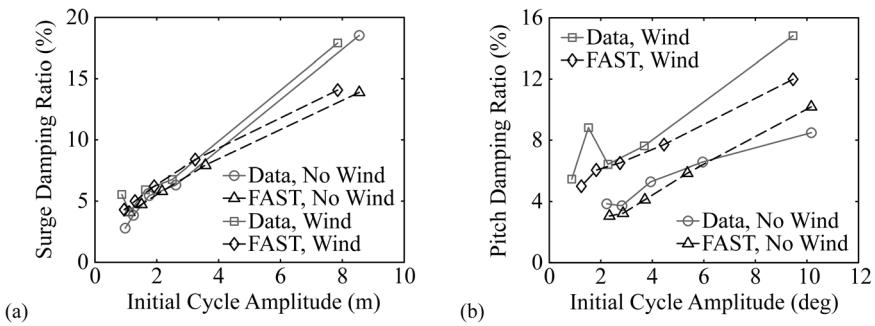

FIG. 11. Comparison of simulation and test data damping ratios for (a) surge and (b) pitch motion for no wind and 11.23 m/s steady wind cases.

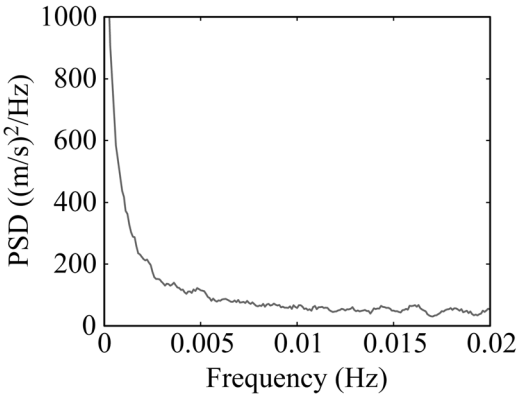

FIG. 12. PSD plot for NPD wind spectrum with mean wind speed of 20.6 m/s at 90 m above SWL.

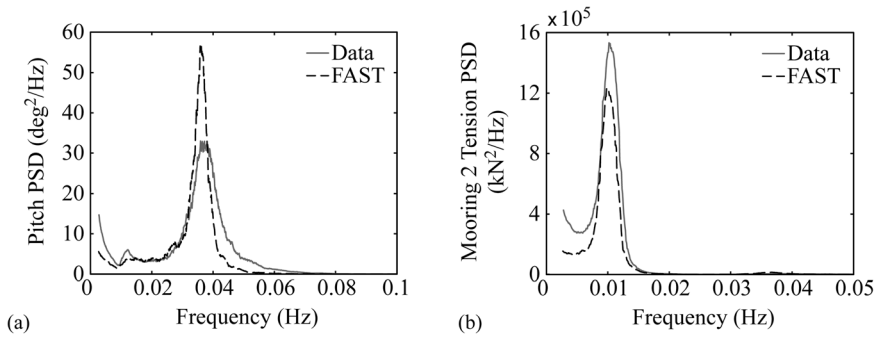

FIG. 13. Comparisons of PSDs from FAST and test data for (a) pitch and (b) mooring line 2 fairlead tension for a dynamic wind-only case with a mean hub-height wind speed of 20.6 m/s.

while Fig. 14 displays sample time-series comparisons. As can be seen in Fig. 13, the PSD comparison is fair for platform pitch with similar total energy; however, the FAST response is more peaked at the platform natural pitch frequency (0.037 Hz) with less response at frequencies immediately above this particular point. Despite this difference in platform-pitch PSD response, Fig. 14 shows good agreement between the FAST simulation and test data time-series consistent with the steady state offset findings in Fig. 10. Regarding the mooring line 2 fairlead tension, the PSD and time-series comparisons given in Figs. 13 and 14, respectively, are also quite favorable. While there was good agreement, FAST generally produces slightly less response for both the PSD and time-series.

In addition to sample PSD and time-series, Table XIV provides statistical comparisons of the FAST simulation and test data for field variables that experience significant excitation for

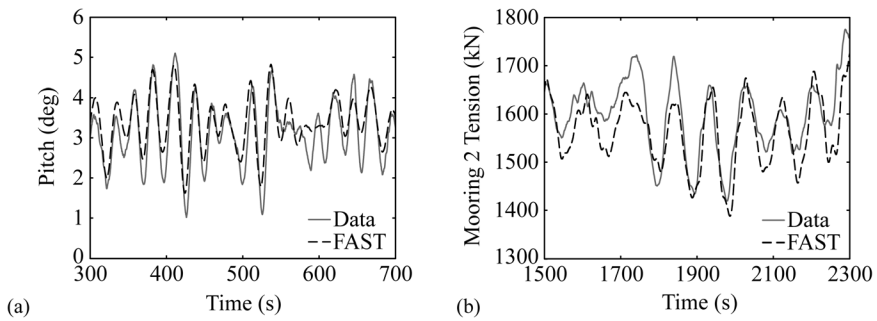

FIG. 14. Comparisons of time-series from FAST and test data for (a) pitch and (b) mooring line 2 fairlead tension for a dynamic wind-only case with a mean hub-height wind speed of 20.6 m/s.

TABLE XIV. Comparison of FAST prediction and test data statistics for a dynamic wind-only case with a mean hub height wind speed of 20.6 m/s.

DOF	Source	Mean	Std. dev.	Maximum	Minimum
Surge (m)	FAST	7.22	0.93	9.96	4.07
	Data	7.26	1.18	10.89	3.64
Pitch (deg)	FAST	3.43	0.69	5.45	0.97
	Data	3.34	0.67	5.65	1.04
Fore-Aft bending (kNm)	FAST	8.45×10^4	1.12×10^4	12.21×10^4	3.66×10^4
	Data	8.09×10^4	1.17×10^4	11.84×10^4	4.03×10^4
Fairlead 2 tension (kN)	FAST	1.58×10^3	0.075×10^3	1.83×10^3	1.35×10^3
	Data	1.64×10^3	0.094×10^3	1.96×10^3	1.36×10^3

this dynamic wind-only condition. After a review of Table XIV, it is clear that the surge, pitch, tower-base bending moment, and mooring line 2 fairlead tension statistics are in very good agreement between FAST and the test data. Of all the comparisons provided, the largest difference is for the platform surge with FAST predicting the maximum value to be 8.54% smaller than the true value. However, the mean platform surge is accurately predicted.

D. Regular waves only

To begin the validation of FAST to test data due to wave excitation, the response of the DeepCwind semi-submersible platform to regular waves in the absence of wind was investigated. Since there was no wind, the blades were feathered and the rotor was parked. Seven different regular waves were considered, the amplitudes and periods of which are given in Table XV. All waves propagated in the positive surge direction. It should be noted that two distinct amplitudes were investigated for periods of 12.1, 14.3, and 20.0 s for the purpose of assessing any nonlinearity in system response. The DeepCwind semi-submersible platform performance in the presence of regular waves is characterized by response amplitude operators (RAOs) magnitudes, which normalize the amplitude of a periodic response of a field variable by the amplitude of the regular wave. In both the time-domain simulation and model test, the RAO values were computed from the nearly harmonic, steady-state response. For FAST, simulations were run for 1600 s to achieve the desired steady-state result.

The RAO magnitudes for surge, heave, pitch, tower-base fore-aft bending moment, and fairlead tension for mooring lines 1 and 2 are given in Fig. 15 for the seven regular waves investigated. Many of the comparisons in Fig. 15 are quite good, as evidenced by FAST's ability to capture the increase in normalized pitch response for a given wave period with increasing wave amplitude. However, there are some notable discrepancies between the FAST simulation and test data. First, the FAST simulation modestly under-predicts the heave RAO for the two 20.0 s cases investigated. Because this period is in close proximity to the DeepCwind semi-submersible's heave natural period (causing some resonance), the normalized response will be

TABLE XV. Regular wave amplitudes and natural periods.

Amplitude (m)	Period (s)
0.96	7.5
3.79	12.1
3.57	14.3
3.79	20.0
5.15	12.1
5.37	14.3
5.56	20.0

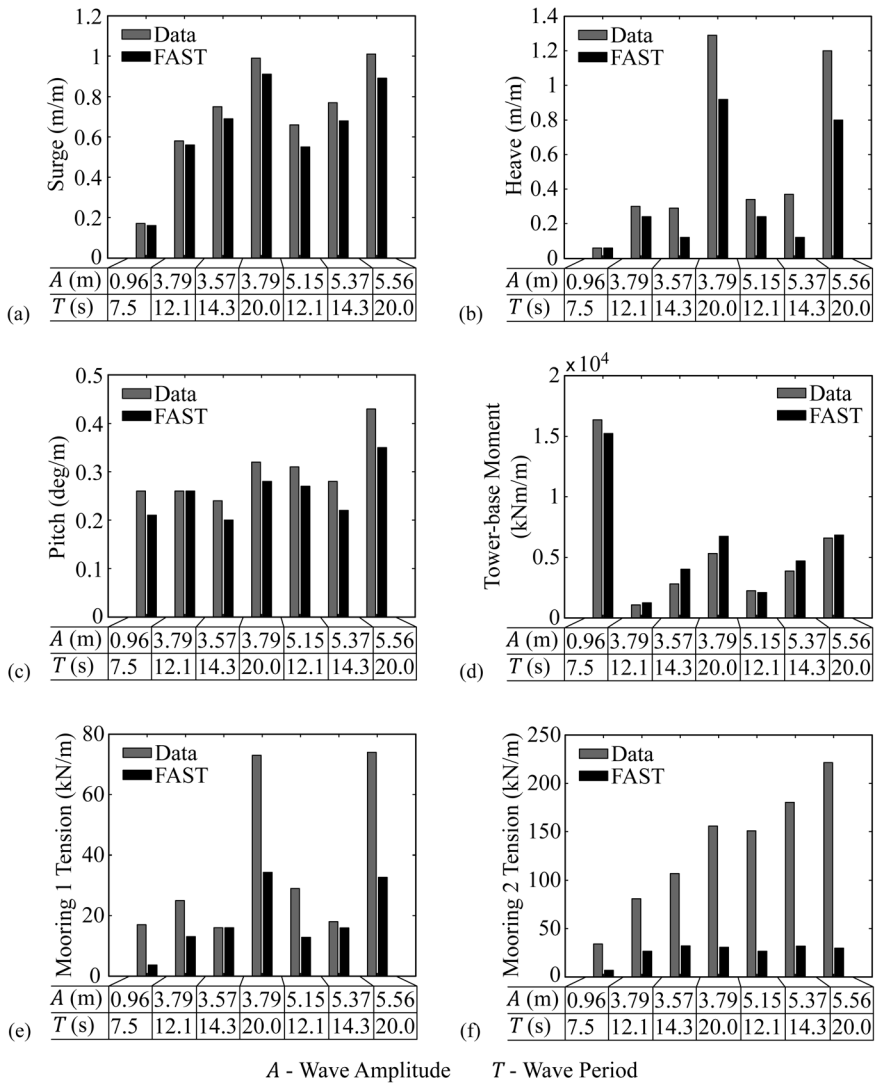

FIG. 15. Comparisons of RAOs from FAST and test data for (a) surge, (b) heave, (c) pitch, (d) tower base fore-aft bending moment, (e) mooring line 1 fairlead tension, and (f) mooring line 2 fairlead tension.

sensitive to system damping. The discrepancy is likely a result of the quadratic damping model employed in this study, which over-predicts the damping in large amplitude heave scenarios at the expense of properly modeling the damping for small to moderate motions. The second discrepancy, which is very significant, is the mooring line fairlead tensions, especially for mooring line 2, which is aligned with the wave propagation direction. For the worst scenario, the 5.56 m amplitude, 20.0 s regular wave, the FAST mooring line 2 fairlead tension RAO is only 13.4% of the test data value. It is suspected that this is caused by the exclusion of dynamic mooring line effects in the simulation, because FAST employs a quasi-static mooring solver. Further investigation would be required to confirm this hypothesis.

E. Irregular waves only

To continue the validation study, the behavior of the DeepCwind semi-submersible platform subjected to a severe irregular wave in the absence of wind was simulated with the calibrated FAST model, and the simulation results were compared to test data. There was no wind, so the blades were feathered and the rotor was parked. The wave that was investigated possessed a broad-band, white noise spectrum, shown in Fig. 16, with a significant wave height of

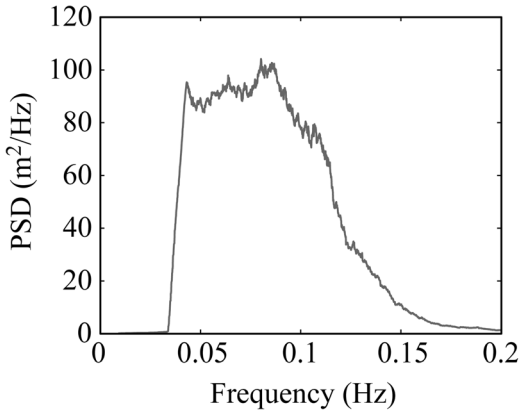

FIG. 16. PSD for 11.3 m significant wave height white noise wave.

11.3 m. This significant wave height is in excess of that corresponding to a 100-year event in the Gulf of Maine.[32] The wave propagated along the positive surge direction. For the 3 h wave, the maximum crest was 12.8 m, the minimum trough was −11.0 m, and the maximum wave height was 21.5 m. The broad-band spectrum utilized here is advantageous for computing RAOs as well as for amplifying, and thus highlighting, the floating wind turbine's response to second-order wave diffraction forces (e.g., see Ref. 45). To make the comparison between FAST and the model test data a fair one, a modified version of FAST was employed that could compute the linear wave diffraction forces directly from the tested wave-elevation time-series.

The first results shown are the FAST simulation and test data RAO magnitude and phase angles for the surge, heave, and pitch DOF in the wave energy range (5–25 s). The plots, given in Fig. 17, show that the motion RAO magnitudes are for the most part quite good.

The same cannot be said, however, of the phase angles in general. This could be a result of the wave measurement, which was located at the undisplaced position, not coinciding with the

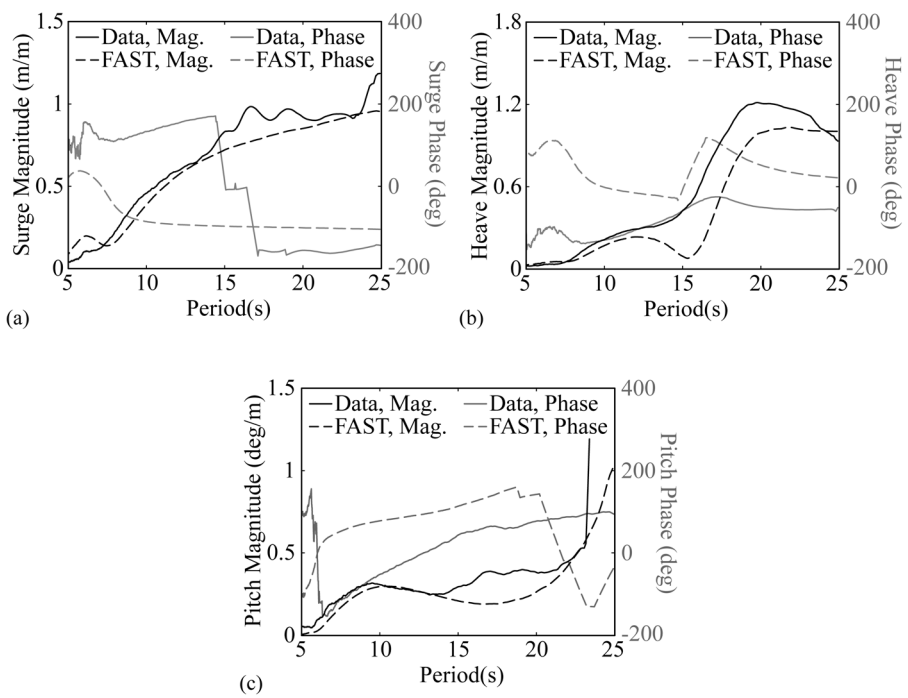

FIG. 17. Comparison of RAO magnitudes and phase angles from FAST and test data for (a) surge, (b) heave, and (c) pitch.

true position of the platform as a result of mean drift forces. Regarding the RAO magnitudes, the worst discrepancy between FAST and the test data occurs in the heave DOF for periods near the resonant system heave period of 17.5 s, with FAST modestly under-predicting the heave response. This observation is consistent with those made for the regular waves investigated.

To further assess FAST's hydrodynamics abilities, PSD comparisons are presented in Fig. 18 for surge, heave, tower-base fore-aft bending moment, and mooring line 2 fairlead tension. Referring to the surge comparison in Fig. 18, it is clear that FAST accurately captures the response in the wave energy range (0.04 to 0.15 Hz); however, the prediction of the second-order difference-frequency associated response at the surge natural period of 0.0093 Hz is very poor. This is understandable because FAST neglects this aspect of the wave loading. Moving to the PSD of the tower-base fore-aft bending moment, it can be seen in Fig. 18 that the comparison is fairly good between the FAST simulation and test data. FAST captures the large response at the platform-pitch natural period of 0.037 Hz, as well as the response in the wave-energy range. This stated, the response at the fore-aft fundamental tower bending frequency of 0.35 Hz is severely under-predicted. If the tower modal damping is reduced to negligible levels, the comparison between FAST and the test data at this frequency improves, capturing nearly one third of the measured response as opposed to less than 10% for the calibrated FAST model. Thus, a partial explanation for the difference may be a poor calibration of the tower modal damping. Another explanation is that second-order sum-frequency wave loads, neglected in FAST, may be sufficient to excite tower motion near the fundamental bending frequency. A further explanation for the large difference may be that dynamic loads from the instrumentation cables, which were attached to an automated following system, may be providing additional excitation of the tower that would not exist for commercial, field-deployed systems, and is not accounted for in this FAST model. The final PSD considered, the mooring line 2 fairlead tension, shows a large discrepancy between the FAST simulation test data over a broad range of frequencies. As can be seen by comparing the surge and mooring tension PSDs in Fig. 18, the relative difference between the FAST simulation and test data are nearly identical in the vicinity of the surge natural frequency of 0.0093 Hz. This indicates that if FAST was able to account for the second-order, difference-frequency associated surge motion, it is likely that

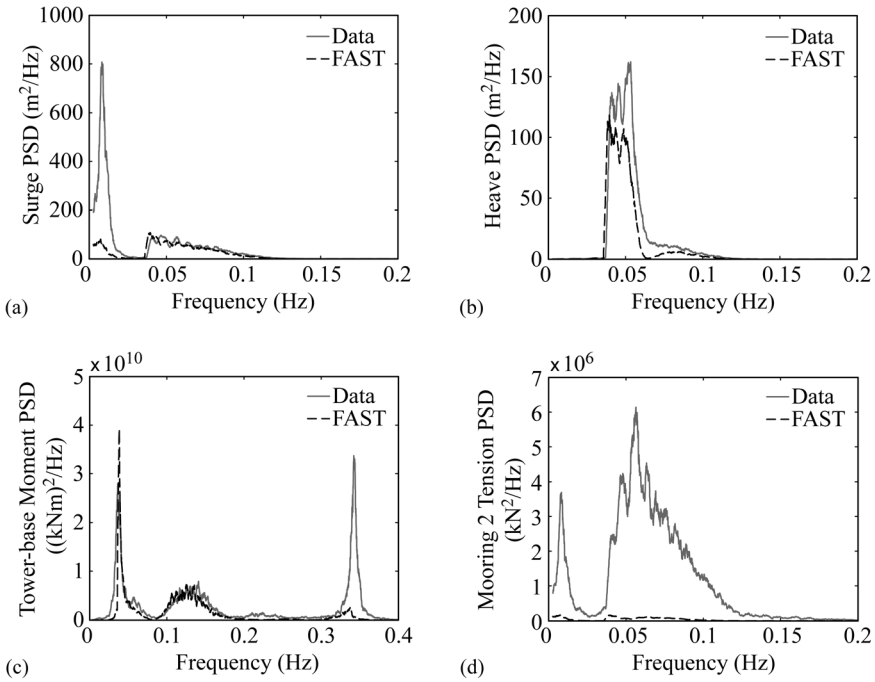

FIG. 18. Comparisons of PSDs from FAST and test data for (a) surge, (b) heave, (c) tower-base fore-aft bending moment, and (d) mooring line 2 fairlead tension for an irregular white noise wave only case with a significant wave height of 11.3 m.

FAST's quasi-static catenary mooring line solver could capture the mooring tension behavior associated with slowly varying drift motion. However, FAST's admirable performance with regard to emulating the correct surge motion response in the wave-energy range does not translate into accurate prediction of mooring tensions in the wave energy frequency range. As can be seen in Fig. 18, the mooring line 2 fairlead tension dynamic response is grossly under-predicted by FAST. This clearly demonstrates that mooring line tension is not arising from platform motion alone and the sharp increase in mooring line 2 fairlead tension response in the wave energy frequency range is likely the result of dynamic mooring effects that are excluded in the FAST simulation. It is suspected that the inclusion of a more sophisticated, finite-element-method based dynamic mooring module (e.g., see Refs. 46 and 47) into FAST might rectify much of the discrepancy between FAST and the test data for mooring tension response in the wave-energy frequency range.

To complement previous results in the section, a comparison of FAST simulation and test data time-series for surge and heave motion is given in Fig. 19. Turning to the surge time-series, it is clear that the higher frequency wave response is captured commendably by FAST; however, the mean drift and slowly-varying response of the real system is visibly ignored. This observation, consistent with previous statements, indicates that the inclusion of mean drift and second-order difference-frequency wave diffraction models into FAST would likely yield high quality hydrodynamic simulations. Moving to the second comparison, the heave time-series are similar in nature, with FAST occasionally under-predicting the magnitude of the heave motion excursion. This is consistent with the heave motion RAO and PSD previously presented. As noted earlier, this is most likely due to too much damping in the FAST model for heave motions with large amplitudes.

To complete this section, a comparison of the simulated and measured statistics for surge, heave, pitch, tower-base fore-aft bending moment, and mooring line 1 and 2 fairlead tensions is given in Table XVI. It is observed from Table XVI that FAST under-predicts the standard deviation and range for the six field variables presented. Other key points worth noting include FAST's inability to predict the surge mean drift position and a maximum mooring line 2 fairlead tension that is only 26.7% of the measured value. This last discrepancy is in part due to FAST estimating insufficient surge motion, with the remainder likely due to a neglect of dynamic mooring effects. Nonetheless, many of the statistical comparisons are fair and differences between the FAST simulation and test data are in keeping with previous observations in this section.

F. Combined dynamic wind and irregular wave

To complete this validation study, a combined dynamic wind and irregular wave case of 3 h in length was studied. The wave and wind were aligned and directed along the positive surge direction. The dynamic wind was the same as that described in Sec. IV C. The wave considered was a 10.5 m significant wave height, 14.3 s peak spectral period wave based on a JONSWAP[48] spectrum, shown in Fig. 20, with a shape parameter of 3.0.

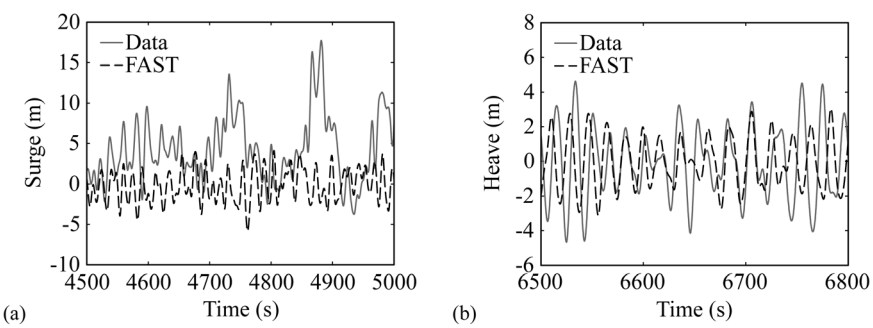

FIG. 19. Comparisons of time-series from FAST and test data for (a) surge and (b) heave for an irregular white noise wave only case with a significant wave height of 11.3 m.

TABLE XVI. Comparison of FAST prediction and test data statistics for an irregular white noise wave only case with a significant wave height of 11.3 m.

DOF	Source	Mean	Std. dev.	Maximum	Minimum
Surge (m)	FAST	−0.14	2.01	8.09	−6.79
	Data	3.78	2.99	18.01	−4.41
Heave (m)	FAST	0.00	1.42	4.27	−4.17
	Data	−0.07	1.73	5.87	−6.50
Pitch (deg)	FAST	−0.01	1.20	4.83	−3.75
	Data	−0.02	1.55	6.94	−6.09
Fore-Aft bending (kNm)	FAST	0.0×10^4	2.40×10^4	9.36×10^4	-10.53×10^4
	Data	0.16×10^4	3.31×10^4	19.89×10^4	-19.49×10^4
Fairlead 1 tension (kN)	FAST	1111	60.05	1338	918.6
	Data	990.6	91.91	1403	431.8
Fairlead 2 tension (kN)	FAST	1105	82.68	1541	879.5
	Data	1344	468.0	5774	95.25

This wave corresponds to a 100-year event in the Gulf of Maine.[32] The wave condition possessed a maximum crest of 13.6 m, a minimum trough of −9.6 m, and a maximum wave height of 22.0 m. Unlike the white noise spectrum wave studied in Sec. IV E, the JONSWAP wave considered here is more representative of a real sea condition. For comparison purposes, the custom FAST tool was again employed such that the wave diffraction forces could be computed based on the wave produced in the wind/wave basin during model testing. It is worth noting that while a sea condition of this magnitude would likely be encountered with much more severe winds that would necessitate a parked or idling turbine, the combination studied here of an operating wind turbine in a severe wave environment is still of interest because it is representative of an IEC design load case[48] (DLC 1.6a).

For comparison, this section will focus primarily on the tower-base fore-aft bending moment; however, statistics will also be given for surge, pitch, and mooring line 2 fairlead tension. The response of the fore-aft bending moment is influenced by most of the relevant physics of interest, including wind, waves, tower structural vibration frequencies, and lastly, second-order difference-frequency diffraction wave forcing. Regarding this last effect and its influence on tower-bending, it should be noted that all platform pitch motion, whether as a result of wind, linear wave, or second-order wave forcing, creates tower-base bending moments as a result of supporting the weight of the heavy wind turbine atop a tilted tower. In addition to comparing FAST and the test data for the combined wind and wave case, the bending moment comparison will also be presented for the dynamic wind only and the JONSWAP wave only.

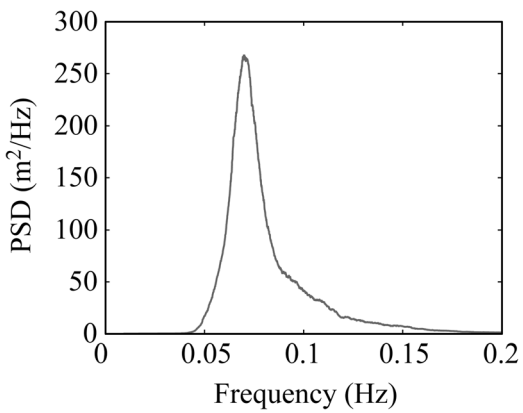

FIG. 20. PSD for 10.5 m significant wave height JONSWAP wave condition.

This will permit assessment of the importance of a few of the wind-only or wave-only deficiencies noted previously, and whether or not they are still present in the combined wind and wave case.

The PSDs of the tower-base fore-aft bending moment for the dynamic wind only, irregular wave only, and combined dynamic wind and irregular wave case are given in Fig. 21. For the dynamic wind only condition, the comparison is very good, with FAST accurately predicting the increase in response resulting from wind-induced system pitch motion (0.037 Hz). Both the FAST and test data show some minor response at the tower fore-aft fundamental bending frequency of 0.35 Hz, with FAST marginally over-predicting the response. Note that Figs. 13 and 14 and Table XIV contain additional plotted results and statistics, respectively, for the dynamic wind only condition used in the combined case.

Moving to the wave-only bending moment PSD, the comparison is fairly good in the wave-energy range (0.05 to 0.2 Hz), but less so outside of these bounds. FAST poorly predicts the sharp rise in bending moment response associated with platform-pitch motion resulting from second-order difference-frequency wave diffraction forces at 0.037 Hz. The response at the fore-aft fundamental bending frequency is also severely under-predicted by FAST, the possible reasons being highlighted in Sec. IV E. On a positive note, the strong correlation between FAST and test data in the wave-energy range is very encouraging because the response for the tower-base fore-aft bending moment is rather complex. Note that in Fig. 21 there is a marked decrease in response near 0.08 Hz, despite the fact that the peak wave energy occurs at 0.07 Hz. This results from the unique platform motion of this system for this particular sea. Despite significant platform motion, the nacelle motion is very low. This results in lower inertial forces at the tower-top and hence, lower tower-base bending moments. As Fig. 21 clearly shows, this behavior is accurately captured by FAST. To continue the discussion of wave-only response to the JONSWAP wave, Table XVII below shows statistics for the field variables of interest. The results comparison is fair, with similar discrepancies and possible explanations as those given for the irregular wave-only study with the 11.3 m significant wave height white noise wave.

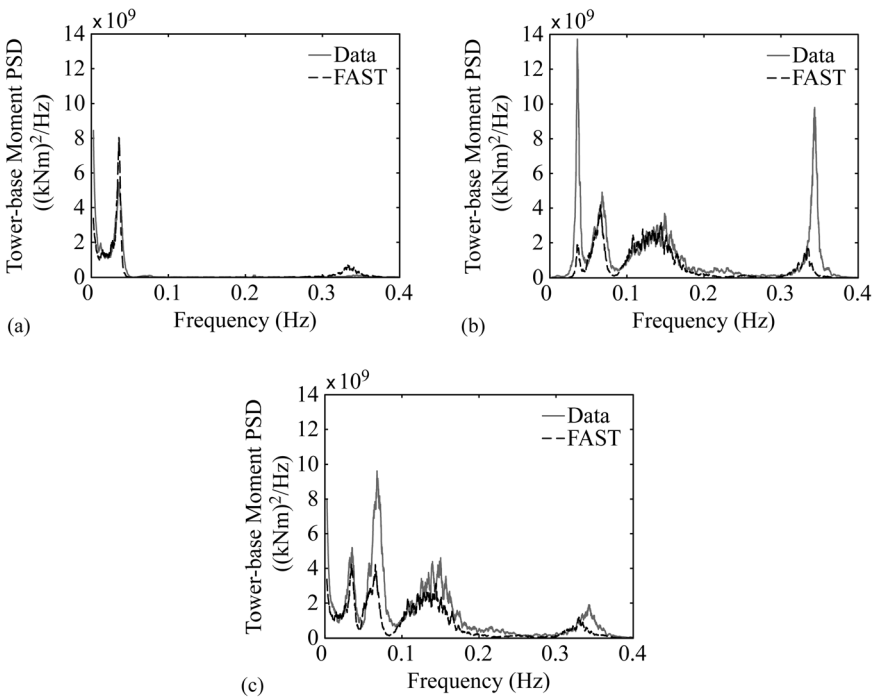

FIG. 21. Comparisons of tower-base fore-aft bending moment PSDs from FAST and test data for (a) 20.6 m/s mean wind speed dynamic wind only, (b) 10.5 m significant wave height irregular wave only, and (c) combined dynamic wind and wave cases.

TABLE XVII. Comparison of FAST prediction and test data statistics for an irregular wave-only case with a significant wave height of 10.5 m.

DOF	Source	Mean	Std. dev.	Maximum	Minimum
Surge (m)	FAST	−0.08	1.75	6.89	−7.37
	Data	2.35	2.37	16.29	−4.98
Pitch (deg)	FAST	0.00	0.68	3.15	−3.10
	Data	−0.06	1.08	4.50	−4.15
Fore-Aft bending (kNm)	FAST	0.0×10^4	1.61×10^4	7.69×10^4	-6.83×10^4
	Data	0.13×10^4	2.14×10^4	17.85×10^4	-13.55×10^4
Fairlead 2 tension (kN)	FAST	1106	75.41	1487	862.0
	Data	1256	406.9	5469	36.05

Moving to the combined dynamic wind and irregular wave condition of Fig. 21, the comparison between FAST and the test data shows a fairly good agreement over the entire range of frequencies investigated. The figure indicates that the tower-base fore-aft bending moment response at the platform-pitch (0.037 Hz) and fundamental tower-bending (0.35 Hz) frequencies is dominated by wind rather than second-order wave diffraction or other effects and is therefore predicted very well by FAST. Over the wave-energy range of 0.05 to 0.2 Hz, FAST captures the appropriate trend in the response, albeit with less energy than measured during testing. Because the measured response in the wave-energy frequency range is greater for the combined wind and wave condition than just for waves alone, the data suggests that the combined case yields additional excitation to the system. This could be caused by wave-induced motion creating additional aerodynamic loads as a result of altering the wind turbine rotor relative velocity at frequencies in the wave energy range. It is possible that this calibrated model of FAST may be unable to capture these higher frequency changes in rotor aerodynamic load as a result of choosing simplistic aerodynamic calculation options, for example, by eliminating the dynamic stall model. By employing a wind turbine model that exploits the full features of FAST's aerodynamic calculation abilities, a better comparison in the wave-energy range could result for the tower-base fore-aft bending moment for the combined dynamic wind and irregular wave case. That aside, this case is much more realistic because it is unlikely the system would see either a high wave or wind loading alone; they would be expected to occur simultaneously. To finish the comparison, Table XVIII presents the statistics for the combined wind and wave case.

While discrepancies are still present for the field variables shown, the presence of the wind loads reduces some of the error compared to the wave-only case. The surge response compares much better in this case, with FAST capturing 76.8% of the mean offset without the inclusion of any second-order wave forcing. The discrepancies in the predicted ranges of the surge, pitch, and tension in mooring line 2 responses are similar to the wave-only case, and the predicted

TABLE XVIII. Comparison of FAST prediction and test data statistics for the combined case consisting of an irregular wave with a significant wave height of 10.5 m and a dynamic wind with a mean hub height wind speed of 20.6 m/s.

DOF	Source	Mean	Std. dev.	Maximum	Minimum
Surge (m)	FAST	7.13	1.81	13.87	0.28
	Data	9.28	2.29	22.26	2.33
Pitch (deg)	FAST	3.42	0.89	6.70	−0.05
	Data	3.49	1.23	8.66	−1.33
Fore-Aft bending (kNm)	FAST	8.44×10^4	1.85×10^4	16.16×10^5	1.76×10^4
	Data	8.45×10^4	2.42×10^4	21.70×10^4	-5.01×10^4
Fairlead 2 tension (kN)	FAST	1580	135.1	2231	1173
	Data	1825	697.6	8109	23.42

range of tower-base bending moments is improved. Overall, FAST demonstrates a fair prediction in this combined wind and wave loading scenario, which is promising.

V. CONCLUSIONS

This work presented the validation of a FAST numerical model of the DeepCwind semi-submersible floating wind turbine system, which supported a slightly altered version of the NREL 5-MW horizontal-axis reference wind turbine using 1/50th-scale model wind/wave basin test data collected at MARIN. Details required for construction of the model are discussed, including system mass, elastic, aerodynamic, and hydrodynamic properties. The calibration procedure is also presented, and includes tuning of the aerodynamics, tower-bending frequencies, and hydrodynamic damping using system identification test data. With the calibrated FAST model complete, a validation study was undertaken comparing FAST predictions to measured test data. Conditions studied included steady and dynamic wind-only cases, platform free-decay motion under steady winds, regular and irregular wave-only conditions, and finally, a combined dynamic wind and irregular wave case. The load cases examined are representative of specific operational and extreme conditions for the Gulf of Maine.

Upon completion of the validation study, a number of important observations were made. For wind-only loading, whether steady or dynamic, FAST predictions agree very well with experimental data, producing similar statistics, PSDs, and time-series. For wave-only cases, FAST simulations captured the linear wave energy frequency response of the DeepCwind semi-submersible well. The mean drift and second-order difference-frequency responses present in the test data, which were occasionally quite strong, were not captured by FAST. Another deficiency discovered included the significant under-prediction of the mooring line fairlead tensions by FAST's quasi-static mooring module. A portion of this deficiency was likely caused in part by the neglect of platform mean and slowly-varying drift forces; however, much of the deficiency was probably caused by dynamic mooring effects, which FAST is unable to account for. In combined dynamic wind and wave cases, the test data indicated that wind forcing dominated second-order wave and tower-bending frequency effects. Because FAST performed admirably in predicting wind-induced response, the combined wind and wave case studied showed a fairly good agreement between the simulation and test data. This finding signifies that FAST's neglect of second-order wave diffraction effects may only be important in extreme events when the wind turbine blades are feathered and the rotor is parked or idling. A further observation is that a more sophisticated damping model could reduce some discrepancies in the validation studies presented here. One way to achieve this in such a model would be to represent the individual components of the submerged portion of the platform with Morison elements rather than just assigning global damping coefficients to the model.

Aside from possible improvements for the numerical model, the validation studies also revealed potential areas of improvement for experimental set-up and procedures. The cable bundle used to transmit data from the model to the computers added stiffness to both the tower and the surge motion DOF that would never exist in a full-scale, commercial system. Wireless data transmission would eliminate the need for this cable bundle altogether. The tower could also be improved because the one used here was composed of multiple cross sections. It would be more desirable to have a uniform or linearly tapered cross section along the length of the tower to make distributed properties continuous (both mass and elastic) and hence easier to quantify and model. Another experimental improvement would be to modify the wind turbine so the rotor thrust is correct at properly scaled wind speeds. One way this could be addressed is through the use of different wind blade designs that perform better in lower Reynolds number regimes. Not having to increase wind speeds to achieve proper thrust values would also reduce the aerodynamic drag on the tower and support structure that is currently ignored by FAST; this would yield better comparisons.

In conclusion, this validation study has found FAST to perform well in predicting the coupled aero-hydro-elastic response of the DeepCwind semi-submersible floating wind turbine. The results indicate that the inclusion of second-order wave diffraction and mooring dynamic physics into

FAST, the formulations and implementations for which are readily available, would create an accurate and powerful tool for the design and analysis of floating wind turbines.

ACKNOWLEDGMENTS

The authors gratefully acknowledge the financial support from the Department of Energy through DeepCwind Grants DE-EE0002981 and DE-EE0003728 and National Renewable Energy Laboratory Grant DE-AC36-08GO28308, the National Science Foundation through Grant IIP-0917974 and the University of Maine. In addition, the expertise and support of MARIN in conducting the model test is greatly appreciated.

[1]J. M. Jonkman and M. L. Buhl, Jr., "FAST User's Guide," NREL Technical Report No. EL-500-38230, August 2005.
[2]J. M. Jonkman, "Dynamics modeling and loads analysis of an offshore floating wind turbine," NREL Technical Report No. TP-500-41958, November 2007.
[3]J. M. Jonkman and M. L. Buhl, Jr., "Loads analysis of a floating offshore wind turbine using fully coupled simulation," NREL Technical Report No. CP-500-41714, June 2007.
[4]G. Bir and J. Jonkman, "Aeroelastic instabilities of large offshore and onshore wind turbines," in Proceedings of the 2007 Science of Making Torque from Wind Conference, Journal of Physics: Conference Series, 2007, Vol. 75, issue 1.
[5]J. M. Jonkman, "Influence of control on the pitch damping of a floating wind turbine," in Proceedings of the 2008 ASME Wind Energy Symposium, Reno, Nevada, USA, 7–10 January 2008.
[6]J. M. Jonkman and D. Matha, "Dynamics of offshore floating wind turbines—analysis of three concepts," Wind Energy **14**(4), 557–569 (2011).
[7]A. N. Robertson and J. M. Jonkman, "Loads analysis of several offshore floating wind turbine concepts," in *Proceedings the of 21st International Offshore and Polar Engineering Conference, Maui, Hawaii, USA, 19–24 June 2011* (ISOPE, 2011), pp. 443–450.
[8]A. Jain, A. N. Robertson, J. M. Jonkman, A. J. Goupee, and R. W. Swift, "FAST code verification of scaling laws for DeepCwind floating wind system tests," in *Proceedings of the 22nd International Offshore and Polar Engineering Conference, Rhodes, Greece, 17–22 June 2012* (ISOPE, 2012), pp. 355–365.
[9]L. Wang and B. Sweetman, "Simulation of large-amplitude motion of floating wind turbine using conservation of momentum," Ocean Eng. **42**, 155–164 (2012).
[10]M. A. Lackner and M. A. Rotea, "Passive structural control of offshore wind turbines," Wind Energy **14**(3), 373–388 (2011).
[11]M. A. Lackner and M. A. Rotea, "Structural control of floating wind turbines," Mechatronics **21**(4), 704–719 (2011).
[12]G. M. Stewart and M. A. Lackner, "The effect of actuator dynamics on active structural control of offshore wind turbines," Eng. Struct. **33**(5), 1807–1816 (2011).
[13]S. Shim and M. H. Kim, "Rotor-floater-tether coupled dynamic analysis of offshore floating wind turbines," in Proceedings of the 18th International Offshore and Polar Engineering Conference, Vancouver, British Columbia, Canada, 6–11 July 2008.
[14]C. Cermelli, D. Roddier, and A. Aubult, "WindFloat: A floating foundation for offshore wind turbines—Part II: hydrodynamics analysis," in *Proceedings of the ASME 28th International Conference on Ocean, Offshore and Arctic Engineering, Honolulu, Hawaii, USA, 31 May–5 June 2009* (ASME, 2009), pp. 135–143.
[15]D. Roddier, C. Cermelli, A. Aubault, and A. Weinstein, "WindFloat: A floating foundation for offshore wind turbines," J. Renewable Sustainable Energy **2**(3), 033104 (2010).
[16]K. Iijima, J. Kim, and M. Fujikubo, "Coupled aerodynamic and hydroelastic analysis of an offshore floating wind turbine system under wind and wave loads," in *Proceedings of the ASME 29th International Conference on Ocean, Offshore and Arctic Engineering*, Shanghai, *China, 6–11 June 2010* (ASME, 2010), pp. 241–248.
[17]Y. H. Bae and M. H. Kim, "Rotor-floater-mooring coupled dynamic analysis of mini TLP-type offshore floating wind turbines," in *Proceedings of the 29th ASME International Conference on Ocean, Offshore and Arctic Engineering, Shanghai, China, 6–11 June 2010* (2010), pp. 491–498.
[18]M. Masciola, A. Robertson, J. Jonkman, and F. Driscoll, "Investigation of a FAST-OrcaFlex coupling module for integrating turbine and mooring dynamics of offshore floating wind turbines," in Proceedings of the 2011 International Conference on Offshore Wind Energy and Ocean Energy, Beijing, China, 31 October–2 November 2011.
[19]J. M. Jonkman and M. L. Buhl, Jr., "Development and verification of a fully coupled simulator for offshore wind turbines," in Proceedings of the 45th AIAA Aerospace Sciences Meeting and Exhibit, Wind Energy Symposium, Reno, Nevada, USA, 8–11 January 2007.
[20]J. M. Jonkman, "Dynamics of offshore floating wind turbines—model development and verification," Wind Energy **12**(5), 459–492 (2009).
[21]J. Jonkman and W. Musial, IEA Wind Task 23 Subtask 2, Final Report, IEA Wind, 31 March 2010.
[22]F. G. Nielsen, T. D. Hanson, and B. Skaare, "Integrated dynamic analysis of floating offshore wind turbines," in *Proceedings of the 25th International Conference on Offshore Mechanics and Arctic Engineering, Hamburg, Germany, 4–9 June 2006* (ASME, 2006), pp. 671–679.
[23]N. X. Ren, Y. G. Li, and J. P. Ou, "The effect of additional mooring chains on the motion performance of a floating wind turbine with a tension leg platform," Energies **5**(4), 1135–1149 (2012).
[24]G. Stewart, M. Lackner, A. Roberston, A. Jonkman, and A. Goupee, "Calibration and validation of a FAST floating wind turbine model of the DeepCwind scaled tension-leg platform," in *Proceedings of the 22nd International Offshore and Polar Engineering Conference, Rhodes, Greece, 17–22 June 2012* (2012), pp. 380–387.
[25]J. R. Browning, J. Jonkman, A. Robertson, and A. J. Goupee, "Calibration and validation of the FAST dynamic simulation tool for a spar-type floating offshore wind turbine," in Proceedings of 2012 the Science of Making Torque from Wind Conference, Oldenburg, Germany, 9–11 October 2012.

[26]A. J. Goupee, B. J. Koo, K. Lambrakos, and R. W. Kimball, "Model tests for three floating wind turbine concepts," in Proceedings of the 2012 Offshore Technology Conference, Houston, Texas, USA, 30 April 2012–3 May 2012.
[27]A. J. Goupee, B. Koo, R. W. Kimball, K. F. Lambrakos, and H. J. Dagher, "Experimental comparison of three floating wind turbine concepts," in Proceedings of the 31st ASME International Conference on Offshore Mechanics and Arctic Engineering, Rio de Janeiro, Brazil, 1–6 July 2012.
[28]B. Koo, A. J. Goupee, K. Lambrakos, and R. W. Kimball, "Model tests for a floating wind turbine on three different floaters," in Proceedings of the 31st ASME International Conference on Offshore Mechanics and Arctic Engineering, Rio de Janeiro, Brazil, 1–6 July 2012.
[29]W. L. Moon III and C. J. Nordstrom, "Tension leg platform turbine: A unique integration of mature technologies," in *Proceedings of the 16th Offshore Symposium, Houston, Texas, USA, 9 February 2010* (Texas Section of the Society of Naval Architects and Marine Engineers, 2010), pp. A25–A34.
[30]J. Jonkman, "Definition of the floating system for Phase IV of OC3," NREL Technical Report No. TP-500-47535, May 2010.
[31]J. M. Jonkman, S. Butterfield, W. Musial, and G. Scott, "Definition of a 5-MW reference wind turbine for offshore system development," NREL Technical Report No. TP-500-38060, February 2007.
[32]University of Maine and James W. Sewall Company, Maine Deepwater Offshore Wind Report, February 2011.
[33]H. R. Martin, R. W. Kimball, A. M. Viselli, and A. J. Goupee, "Methodology for wind/wave basin testing of floating offshore wind turbines," in Proceedings of the 31st ASME International Conference on Offshore Mechanics and Arctic Engineering, Rio de Janeiro, Brazil, 1–6 July 2012.
[34]H. R. Martin, "Development of a scale model wind turbine for testing of offshore floating wind turbine systems," M.S. Thesis, University of Maine, 2011.
[35]O. M. Faltinsen, *Sea Loads on Ships and Offshore Structures* (Cambridge University Press, Cambridge, United Kingdom, 1990).
[36]J. N. Newman, *Marine Hydrodynamics* (The MIT Press, Cambridge, Massachusetts, USA, 1997).
[37]C. H. Lee and J. N. Newman, *WAMIT® User Manual, Versions 6.4, 6.4PC, 6.3S, 6.3S-PC* (WAMIT, Inc., Chestnut Hill, Massachusetts, USA, 2006).
[38]*Multisurf 8.0, Version 8.0* (AeroHydro, Inc., Southwest Harbor, Maine, USA 2011).
[39]M. Drela, "XFOIL: An analysis and design system for low Reynolds number airfoils," in Conference on Low Reynolds Number Airfoil Aerodynamics, University of Notre Dame, 5–7 June 1989.
[40]C. Hansen, NWTC Design Codes: AirfoilPrep, http://wind.nrel.gov/designcodes/preprocessors/airfoilprep/, accessed 6 August 2012.
[41]K. Deb, *Multi-Objective Optimization Using Evolutionary Algorithms* (John Wiley & Sons, Chichester, West Sussex, England 2001).
[42]R. D. Cook, D. S. Malkus, M. E. Plesha, and R. J. Witt, *Concepts and Applications of Finite Elment Analysis*, 4th ed. (John Wiley & Sons, Hoboken, New Jersey, USA, 2002).
[43]J. S. Bendat and A. G. Piersol, *Engineering Applications of Correlation and Spectral Analysis* (John Wiley & Sons, New York, New York, USA, 1980).
[44]API Recommended Practice 2A-WSD, *Recommended Practice for Planning, Designing and Constructing Fixed Offshore Platforms—Working Stress Design*, 21st ed. (API Publishing Services, 2000).
[45]M. H. Kim and D. K. P. Yue, "Sum- and difference-frequency wave loads on a body in unidirectional Gaussian seas," J. Ship Res. **35**(2), 127–140 (1991).
[46]D. L. Garrett, "Dynamic analysis of slender rods," J. Energy Resour. Technol. **104**, 302–306 (1982).
[47]J. R. Paulling and W. C. Webster, "A consistent, large-amplitude analysis of the coupled response of a TLP and tendon system," in *Proceedings of the 5th ASME International Conference on Offshore Mechanics and Arctic Engineering, Tokyo, Japan, 13–18 April, 1986* (ASME, 1986), pp. 126–133.
[48]IEC 61400-3, *Wind Turbines—Part 3: Design Requirements for Offshore Wind Turbines* (2009).